



HAL
open science

Numerical simulation of propagation problems on the sphere with a compact scheme

M. Brachet, Jean-Pierre Croisille

► **To cite this version:**

M. Brachet, Jean-Pierre Croisille. Numerical simulation of propagation problems on the sphere with a compact scheme. 2018. hal-01803633v1

HAL Id: hal-01803633

<https://hal.science/hal-01803633v1>

Preprint submitted on 30 May 2018 (v1), last revised 2 Jul 2019 (v2)

HAL is a multi-disciplinary open access archive for the deposit and dissemination of scientific research documents, whether they are published or not. The documents may come from teaching and research institutions in France or abroad, or from public or private research centers.

L'archive ouverte pluridisciplinaire **HAL**, est destinée au dépôt et à la diffusion de documents scientifiques de niveau recherche, publiés ou non, émanant des établissements d'enseignement et de recherche français ou étrangers, des laboratoires publics ou privés.

NUMERICAL SIMULATION OF PROPAGATION PROBLEMS ON THE SPHERE WITH A COMPACT SCHEME

M. BRACHET AND J.-P. CROISILLE†‡

ABSTRACT. We consider propagation problems on the sphere and their approximation by a compact finite difference scheme. The scheme used in this study uses the Cubed Sphere, a particular spherical grid with logically Cartesian structure. A central role is played by the standard one dimensional Hermitian derivative [22]. This compact scheme operates along great circles, thus avoiding any one sided compact scheme. [10, 11]. The scheme is centered. A simple high frequency filter is added to reinforce the stability. The final scheme is reminiscent of compact schemes in Computational Aeroacoustics or in turbulence Direct Numerical Simulation. Numerical results on a broad series of numerical test cases in climatology are presented, including linear convection problems, the linearized shallow water equations and the non linear shallow water equations. The results demonstrate the interest of the present approach in a variety of situations arising in numerical climatology.

Keywords: Cubed-Sphere grid - Compact finite difference scheme - Hermitian derivative - Vortex propagation

1. INTRODUCTION

In this paper we consider propagation equations on the sphere which are of interest in climatology. The considered partial differential equations are related to the spherical Shallow Water equations (SWE). The SWE model represents a reference hyperbolic system to be solved in spherical geometry [15]. A second problem (LSWE) consists of the linearized SWE around an atmosphere at rest. This problem represents a fundamental wave model on the sphere. It is of great importance in climatology and oceanography. On this topic, refer to the recent monograph [25].

In the past twenty years, the SWE and LSWE equation have been the source of many efforts to adapt to numerical climatology the conservative methods commonly used in numerical gas dynamics. This is in particular the case of the finite volume method [7, 35], or the Discontinuous Galerkin method [3]. In this paper, we address another approach, namely the particular finite difference scheme introduced in [10, 11]. This scheme is compact in the sense of [8, 22]. Among the classical methods for fluid flows, it is strongly related to the difference schemes in Computational Aeroacoustics [37, 33, 6] and in turbulence simulation [21]. The novelty lies in the fact that the approximation procedure operates on the Cubed Sphere at the global level. Since the scheme is compact, there is the non locality problem related to the Hermitian derivative. This problem is traditionally handled by mean of a one-sided scheme at near boundary grid points. Here boundary points are avoided by using a particular set of great circles as the geometric basis for the compact scheme. The scheme is centered with one value per gridpoint. Finally, a linear high frequency filter is added for stabilization. Note that our approach is different from other works which use FD schemes in numerical climatology as [2, 14].

Three convective models are considered in this paper:

- The advection equation [38]:

$$(1) \quad \frac{\partial h(t, \mathbf{x})}{\partial t} + \mathbf{c}(t, \mathbf{x}) \cdot \nabla_T h(t, \mathbf{x}) = 0$$

The velocity $\mathbf{c}(t, \mathbf{x})$ is a prescribed tangential vector field representing the wind. The scalar function $h(t, x)$ typically represents the density of a pollutant convected by a wind with velocity \mathbf{c} . The

Date: May, 10 2018.

numerical solution is compared to the analytical solution, which is available by the method of characteristics in particular cases. This permits to evaluate, not only the dissipation and the dispersion, but also the long time behaviour of the scheme.

- The Shallow Water model (LSWE) [25, 26] linearized around the constant state of an atmosphere at rest $q_0 = [H, \mathbf{v} = \mathbf{0}]$ is

$$(2) \quad (LSWE) \begin{cases} \frac{\partial \eta(t, \mathbf{x})}{\partial t} + H \nabla_T \cdot \mathbf{v}(t, \mathbf{x}) = S_\eta(t, \mathbf{x}), \\ \frac{\partial \mathbf{v}(t, \mathbf{x})}{\partial t} + g \nabla_T \eta(t, \mathbf{x}) + f(\mathbf{x}) \mathbf{n}(\mathbf{x}) \times \mathbf{v}(t, \mathbf{x}) = S_\mathbf{v}(t, \mathbf{x}). \end{cases}$$

This system is sometimes referred to as the Laplace Tidal Equation (LTE). The small perturbations are the height η and the velocity \mathbf{v} . The source terms S_η and $S_\mathbf{v}$ stand for forcing functions. The vector function $f(\mathbf{x}) \mathbf{n}(\mathbf{x}) \times \mathbf{v}$ represents the Coriolis force. This problem still offers many mathematical open questions [25]. Accurate numerical simulations are important to have insight in spherical fluid flows in the linear and nonlinear regime.

- The full SWE system [26] in vector form is

$$(3) \quad (SWE) \begin{cases} \frac{\partial h^*}{\partial t}(t, \mathbf{x}) + \nabla_T \cdot (h^*(t, \mathbf{x}) \mathbf{v}(t, \mathbf{x})) = 0 \\ \frac{\partial \mathbf{v}}{\partial t}(t, \mathbf{x}) + \nabla_T \left(\frac{1}{2} |\mathbf{v}(t, \mathbf{x})|^2 + gh(t, \mathbf{x}) \right) + (f(\mathbf{x}) + \zeta(t, \mathbf{x})) \mathbf{n}(\mathbf{x}) \times \mathbf{v}(t, \mathbf{x}) = \mathbf{0} \end{cases}$$

where $\zeta = (\nabla_T \times \mathbf{v}) \cdot \mathbf{n}$ is the *relative vorticity* and $h^* = h - h_s$ with h_s the bottom topography function.

For these three models, and for the numerical cases considered, we show that our centered compact scheme compares favourably with conservative upwind methods, such as the finite volume method [35] or the Discontinuous Galerkin method [23, 3]. Our scheme is a priori not conservative, so we carefully evaluate how evolve the integral values that are preserved at the continuous level. Conserved quantities are of two kinds. There are first the primary conservative quantities, which are by construction preserved by conservative methods. In (3) the primary conserved quantities are the mass and the total energy. However derived quantities such as the relative vorticity or the potential enstrophy are important to conserve as well. There is no guarantee that conservative methods actually preserve such quantities. In fact, it is well known that finite volume methods can excessively dissipate vorticity for large times. This is why the conservation properties of our scheme are numerically analyzed as a whole, without distinction between primary and derived quantities. As we shall see, our scheme performs well regarding conservation for all conserved integral quantities.

Regarding numerical diffusion, we rely on a linear filtering, which aims to remove the +1/-1 mode attached to the grid. It was found that the test cases considered in Sec. 3 do not require more advanced numerical viscosity. In particular, hyperviscosity models, [9] were found not necessary. Similarly, advanced nonlinear filtering such as [39] are not used as well.

The outline of the paper is as follows. In Sec. 2, we recall the background of our approach along the lines of [10, 11]. In particular we give the details of the centered approximation of the gradient, the divergence and the vorticity. In Sec. 3, numerical results on a broad series of test cases involving (1), (2) and (3) are presented. Finally, in Sec. 4 a numerical analysis of the basic compact scheme is carried out on the model of the linear advection equation with periodic setting. This includes a convergence analysis of the standard fourth order compact scheme and a stability matrix analysis of the fully discrete scheme, including filtering. This short section aims to bring some support for the compact scheme on the sphere that is used.

All the computations were performed in *matlab* on a desktop computer.

2. CENTRAL COMPACT DIFFERENCING ON THE CUBED SPHERE

In this section, we review the basics of our compact scheme, which uses the Cubed Sphere grid as geometric primitive. This scheme uses a particular property of the Cubed Sphere, the fact that coordinate lines are great circles sections. These great circles are used to operate the compact differentiation. Here we use the standard

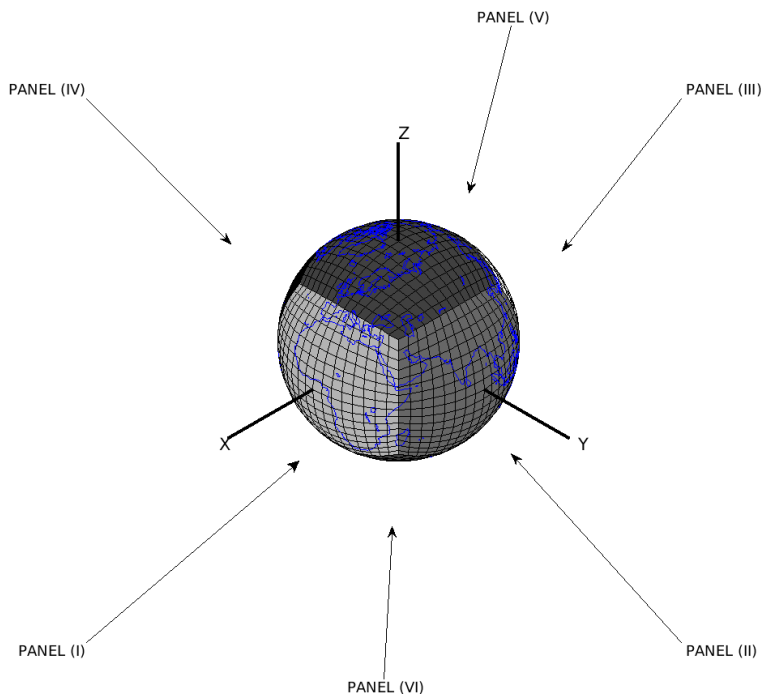


FIGURE 1. The Cubed Sphere with resolution parameter $N = 16$. The number of gridpoints is $6N^2 + 2$, (1538 in this case). The four panels (I), (II), (III) and (IV) are located around the equatorial plane $z = 0$. The labels of the north and south panels are (V) and (VI) respectively.

fourth order Hermitian scheme. This provides accurate approximations to the gradient, the divergence and the vorticity. Higher order schemes were found unnecessary to obtain better numerical results.

2.1. The Cubed Sphere. The Cubed Sphere [30] is a spherical grid widely used in numerical climatology. A modern presentation was given in [29]. It is composed of six panels labeled with $k = (I), (II), (III), (IV), (V)$ and (VI) . Each panel matches the face of a cube and supports a Cartesian grid of size $(N + 1) \times (N + 1)$. The coordinate system on a panel is called (ξ, η) . The angle ξ (resp. η) represents the angle along the "horizontal" (resp. "vertical") equator. The Cubed Sphere is represented in Fig. 1 and a typical panel is shown in Fig. 2. The gridpoints in panel k are denoted $\mathbf{s}_{i,j}^k$. The integer i (resp. j) denotes the index in the ξ direction (resp. η) direction. The points $\mathbf{s}_{i,j}^k$ $-N/2 \leq i, j \leq N/2$ and $(I) \leq k \leq (VI)$ are where the discrete data are located. The spatial steps are identical in the ξ and η directions with resolution

$$(4) \quad \Delta\xi = \Delta\eta = \frac{\pi}{2N} = \Delta.$$

The Cubed Sphere has the symmetries of a Cube [29].

We refer to [19, 12] for works where the Cubed Sphere is used in frameworks different from climatology.

2.2. Great circles on the Cubed Sphere. The spatial approximation used in this paper is based on the standard Hermitian derivative. Consider a function $f(\mathbf{x})$ on the sphere \mathbb{S}_a with radius a . Consider the data $f_{i,j}^k = f(\mathbf{s}_{i,j}^k)$. For j_0 fixed, the Hermitian derivative $\delta_\xi^H f_{i,j_0}^k$ is obtained by

$$(5) \quad \frac{1}{6}\delta_\xi^H f_{i-1,j_0} + \frac{2}{3}\delta_\xi^H f_{i,j_0} + \frac{1}{6}\delta_\xi^H f_{i+1,j_0} = \frac{f_{i+1,j_0} - f_{i-1,j_0}}{2\Delta\xi}.$$

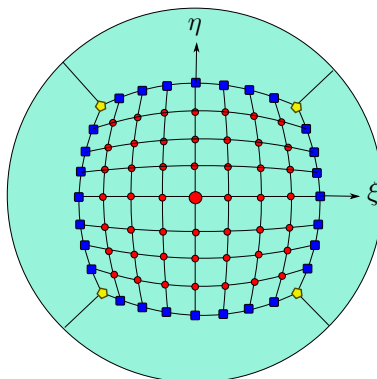


FIGURE 2. Frontal view of a panel. The points of a typical panel of the Cubed-Sphere are classified in three categories: (i) $(N - 1)^2$ circles correspond to the *internal* points; (ii) $4(N - 1)$ squares correspond to the *edge* points ; (iii) 4 pentagons correspond to the *corner* points. The equatorial angles (ξ, η) are such that $-\pi/4 \leq \xi, \eta \leq \pi/4$, with origin at the center of the panel.

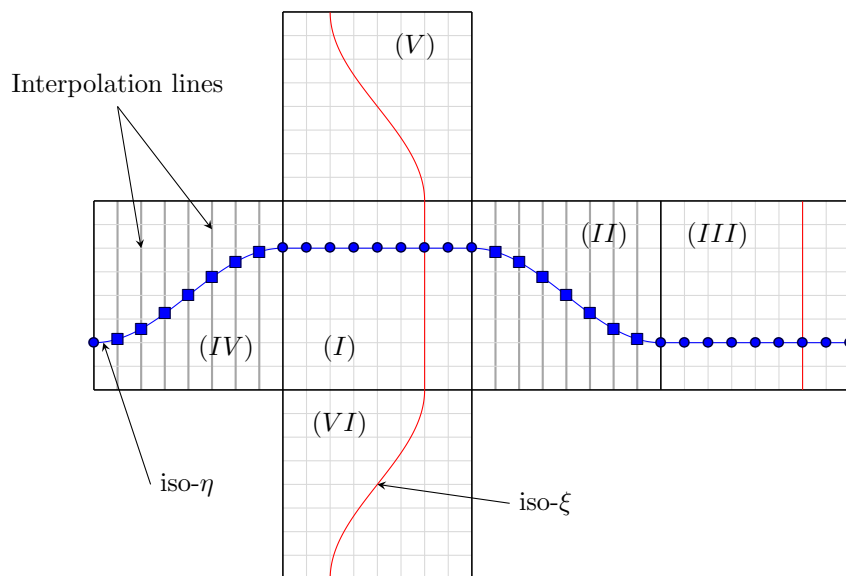
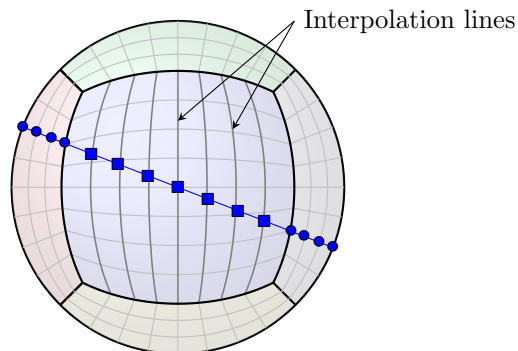


FIGURE 3. Two typical great circles associated to coordinate lines along the Cubed Sphere. Compact differencing is carried out along each circle, giving one-dimensional approximate derivatives. Points marked with circles correspond to gridpoints where discrete values are located. In the contrary, values must be interpolated at points marked with squares.

The truncation error for $\delta_\xi^H f_{i,j_0}$ satisfies

$$(6) \quad \delta_\xi^H f_{i,j_0} - \partial_\xi f(\mathbf{s}_{i,j_0}^k) = -\frac{1}{180} \Delta \xi^4 \partial_\xi^{(5)} f(\mathbf{s}_{i,j_0}^k) + O(\Delta \xi^6).$$

The main point is that the formula (5) is used along a *full great circle*. This means that the ξ - coordinate attached to panel (I) is extended to the full sphere. Therefore there is no one sided compact formula involved at any point. Consider for example in Fig. 3 the great circle marked with points. This circle crosses panels (I), (II), (III) and (IV). It coincides with coordinate lines in panels (I) and (III). In panels (II) and



Panel (II)

FIGURE 4. Frontal view of panel (II) with the great circle in Fig. 3. The points marked with squares are located on panel (II). They do not belong to the grid (except several of them). The value assigned to each point is deduced by a cubic spline interpolation along each vertical line. This gives a 4th. order approximation at each of these points. Doing the same on panel (IV), each point on the circle carries a value, either exact or 4th. order accurate. Applying the Hermitian derivative (5) at these points gives an "almost" 4th. order derivative at points on panels (I) and (III). This procedure is repeated along a set of great circles covering the Cubed Sphere.

(IV) it does not coincide with coordinate lines. Based on the data on the Cubed Sphere $f_{i,j}^k$, one calculates Hermitian derivatives along this circle. This is operated as follows. First a suitable set of points \mathbf{m}_p is defined on this circle. Second, values f_p deduced from $f_{i,j}^k$ are assigned to these points. And third, $\delta_{\Delta}^H f_p$ is calculated by (5). The same calculation is performed in the η - direction. These calculations are repeated in the six panels. At this point, we have at hand approximations $\delta_{\xi}^H f_{i,j}^k$ and $\delta_{\eta}^H f_{i,j}^k$ at each point $\mathbf{s}_{i,j}^k$ of the grid. The approximate gradient of the function f is then deduced as follows. On the panel k , the local basis $(\mathbf{g}_{\xi}, \mathbf{g}_{\eta})$ is

$$(7) \quad \mathbf{g}_{\xi}(\mathbf{x}) = \frac{\partial \mathbf{x}}{\partial \xi}, \quad \mathbf{g}_{\eta}(\mathbf{x}) = \frac{\partial \mathbf{x}}{\partial \eta}.$$

Let $f(\mathbf{x})$ be a function defined on \mathbb{S}_a . We denote by f^* the restriction of f to the grid points:

$$(8) \quad (f^*)_{i,j}^k = f(\mathbf{s}_{i,j}^k).$$

The gradient of $f(\mathbf{x})$ is expressed in terms of the dual basis $(\mathbf{g}^{\xi}, \mathbf{g}^{\eta})$ by

$$(9) \quad \nabla_T f(\mathbf{x}) = \frac{\partial f}{\partial \xi}(\mathbf{x}) \mathbf{g}^{\xi}(\mathbf{x}) + \frac{\partial f}{\partial \eta}(\mathbf{x}) \mathbf{g}^{\eta}(\mathbf{x}).$$

Using the two approximate values

$$(10) \quad \frac{\partial f}{\partial \xi}(\mathbf{s}_{i,j}^k) \simeq \delta_{\xi}^H f_{i,j}^k, \quad \frac{\partial f}{\partial \eta}(\mathbf{s}_{i,j}^k) \simeq \delta_{\eta}^H f_{i,j}^k,$$

a natural approximate gradient $\nabla_{T,\Delta}(f^*)_{i,j}^k$ is defined by (we note $\Delta = \Delta\xi = \Delta\eta$):

$$(11) \quad \nabla_{T,\Delta}(f^*)_{i,j}^k = \delta_{\xi}^H (f^*)_{i,j}^k \mathbf{g}^{\xi}(\mathbf{s}_{i,j}^k) + \delta_{\eta}^H (f^*)_{i,j}^k \mathbf{g}^{\eta}(\mathbf{s}_{i,j}^k).$$

The precise computational procedure proceeds in four steps described in the Algorithm 1 hereafter. Consider again in Fig. 3 the circle marked with points. This circle corresponds to some iso- η line $\eta = \eta_0$ in panel (I). The main point is the extension of the ξ coordinate from the panel (I) to the full circle. This is detailed in the steps 1 and 2 of Algorithm 1. As already said there is a calculation in the ξ direction and a calculation in

the η direction for the six panels, thus 12 calculation in all. However, due to the spherical symmetry, there is in fact only 6 calculations so that Algorithm 1 is applied to the ξ and η coordinate lines only in panels (I), (II) and (V). Overall, a set of $6N$ great circles, covering the Cubed Sphere, are used. Finally, the values $\delta_{\xi}^H(f^*)_{i,j}^k$ and of $\delta_{\eta}^H(f^*)_{i,j}^k$ are obtained on the six panels and the approximation of the gradient is deduced by (11).

Algorithm 1 : Hermitian derivative along the great circle in the ξ - direction in Fig. 3.

- 1: *Defining the grid on the great circle.* Consider a coordinate great circle based on a coordinate line in panel (I). We set up as follows $4N$ points on this circle (see Fig. 3) $\mathbf{m}_p, p = 0, \dots, 4N$. The periodicity on this circle is expressed by $\mathbf{m}_0 = \mathbf{m}_{4N}$.
 - (1) The first N points $\mathbf{m}_p = \mathbf{s}_{p-N/2, j_0}^{(I)}, p = 0, \dots, N - 1$ are located in panel (I). They belong to the Cubed Sphere and they carry values $f_{p-N/2, j_0}^{(I)}$. They are represented by black circles in Fig. 3.
 - (2) The next N points $\mathbf{m}_p, p = N \dots 2N - 1$ belong to panel (II). They do not belong to the Cubed Sphere. Interpolated data of f must be calculated at these points. They are represented by black squares in Fig. 3. These points play the role of auxiliary points.
 - (3) The next N points $\mathbf{m}_p = \mathbf{s}_{p-N/2, j_0}^{(III)}, p = 2N, \dots, 3N - 1$ belong to panel (III). They belong to the Cubed Sphere and they carry values $f_{i, j_0}^{(III)}$. They are represented by black circles in Fig. 3.
 - (4) The last N points $\mathbf{m}_p, p = 3N \dots 4N - 1$ belong to panel (IV). They do not belong to the Cubed Sphere. Interpolated data of f must be calculated at these points. They are represented by black squares in Fig. 3. As in the panel (II), these points are auxiliary points.
 - 2: *Interpolation step.* In this step data are interpolated from the Cubed-sphere to the points \mathbf{m}_p :
 - (1) In panels (I) and (III), the points marked with black circles belong to the Cubed Sphere. Data $f_{p-N/2, j_0}^{(I)}$ are just copied from the Cubed Sphere to the circle. There is no need of interpolation.
 - (2) In panels (II) and (IV), a spline interpolation is performed as follows (see [10]). The circle crosses vertical iso- ξ lines. A cubic spline interpolation maps the data from the vertical iso- ξ line to the points marked with black squares. This gives a 4th order interpolation for f at these points.
 - 3: *Evaluating the Hermitian derivative on the circle.* All the points $\mathbf{m}_p, 0 \leq p \leq 4N$ now carry values. The discrete derivative $\delta_{\xi}^H f_p$ is evaluated with (5). This provides $4N$ (periodic) values called $\delta_{\xi}^H f_p, 0 \leq p \leq 4N$. The differentiation is operated with respect to the equatorial angle. This angle coincides with the ξ -coordinate in the panel (I) or (III).
 - 4: *Restricting the approximate derivative to coordinate lines.* This step consists in retaining the components $\delta_{\xi}^H f_p$ located on panels (I) and (III) only. These components are stored. They correspond to indices $0 \leq p \leq N$, (panel (I)) and $2N \leq p \leq 3N$, (panel (III)). The values of the derivatives in the panels (II) and (IV) are also an outcome of the calculation. But they are useless since the points there do not belong to the Cubed Sphere. Therefore, they are not stored.
-

2.3. Approximation of differential operators. In Section 2.2 we have shown how to approximate the spherical gradient by (11). Using the same principle, the divergence and the vorticity are approximated. Consider a tangential vector field $\mathbf{v}(\mathbf{x})$. The divergence and curl operators are expressed in local coordinates as [31]

$$(12) \quad \begin{cases} \nabla_T \cdot \mathbf{v} = \partial_\xi \mathbf{v} \cdot \mathbf{g}^\xi + \partial_\eta \mathbf{v} \cdot \mathbf{g}^\eta, & (a) \\ \nabla_T \times \mathbf{v} = \mathbf{g}^\xi \times \partial_\xi \mathbf{v} + \mathbf{g}^\eta \times \partial_\eta \mathbf{v} & (b). \end{cases}$$

Consider the data $\mathbf{v}_{i,j}^k$ on the Cubed Sphere. The discrete divergence and vorticity are defined by

$$(13) \quad \begin{cases} \nabla_{T,\Delta} \cdot \mathbf{v}_{i,j}^k = \delta_\xi^H \mathbf{v}_{i,j}^k \cdot (\mathbf{g}^\xi)_{i,j}^k + \delta_\eta^H \mathbf{v}_{i,j}^k \cdot (\mathbf{g}^\eta)_{i,j}^k, & (a), \\ \nabla_{T,\Delta} \times (\mathbf{v})_{i,j}^k = (\mathbf{g}^\xi)_{i,j}^k \times \delta_\xi^H \mathbf{v}_{i,j}^k + (\mathbf{g}^\eta)_{i,j}^k \times \delta_\eta^H \mathbf{v}_{i,j}^k & (b). \end{cases}$$

According to (6), we expect the discrete derivatives to be fourth order accurate. However, due to the interpolation of the data in Step 2 of Algorithm 1, one may wonder if the accuracy could drop to 3. In fact, the value f_p assigned to point \mathbf{m}_p on the circle satisfies

$$(14) \quad \begin{cases} f_p = f(\mathbf{m}_p) \text{ if } \mathbf{m} \text{ belongs to panels (I) or (III).} \\ f_p = f(\mathbf{m}_p) + O(\Delta^4) \text{ if } \mathbf{m} \text{ belongs to panels (II) or (IV).} \end{cases}$$

Therefore it turns out that

$$(15) \quad (f_{p+1} - f_{p-1})/(2\Delta\xi) = (f(\mathbf{m}_{p+1}) - f(\mathbf{m}_{p-1}))/(2\Delta\xi) + O(\Delta^3),$$

which gives

$$(16) \quad \delta_\xi^H f_p = \partial_\xi f(\mathbf{m}_p) + O(\Delta^3).$$

As a consequence the approximations (11) and (12)_{a,b} are at least $O(\Delta^3)$. In practice however, fourth order accuracy has been numerically observed so far.

Remark 2.1. There is some redundancy in the computation. This is due to the fact that in Algorithm 1, the Hermitian derivative in panel (II) and (IV) are not retained. They just serve as auxiliary variables (or "ghost" values).⁰

2.4. Method of lines. Consider for example the SWE system (3). It is rewritten as

$$(17) \quad \partial_t q(t, \mathbf{x}) = J(q(t, \mathbf{x})),$$

where the function $J(q)$ is

$$(18) \quad J(q) = \begin{bmatrix} -\nabla_T \cdot (h^* \mathbf{v}) \\ -\nabla_T \left(\frac{1}{2} |\mathbf{v}|^2 + gh \right) - (f + \zeta) \mathbf{n} \times \mathbf{v} \end{bmatrix}.$$

According to the method of lines, $J(q)$ is first approximated. Then a time stepping scheme is applied. The function $J(q)$ is approximated using the discrete operators (9) and (13)_{a,b}. The semi discrete scheme is

$$(19) \quad \frac{d\mathbf{q}(t)}{dt} = J_\Delta(\mathbf{q}(t)),$$

where $\mathbf{q} = [q_{i,j}^k]^T$ and $-N/2 \leq i, j \leq N/2$, $(I) \leq k \leq (VI)$. The discrete in space function $J_\Delta(\mathbf{q})$ is

$$(20) \quad J_\Delta(\mathbf{q}) = J_\Delta(h_{i,j}^k, \mathbf{v}_{i,j}^k) = \begin{bmatrix} -\nabla_{T,\Delta} \cdot (h_{i,j}^{*k} \mathbf{v}_{i,j}^k) \\ -\nabla_{T,\Delta} \left(\frac{1}{2} |\mathbf{v}_{i,j}^k|^2 + gh_{i,j}^k \right) - (f_{i,j}^k + \zeta_{i,j}^k) \mathbf{n}_{i,j}^k \times \mathbf{v}_{i,j}^k \end{bmatrix},$$

where $\zeta_{i,j}^k = (\nabla_{T,\Delta} \times \mathbf{v}_{i,j}^k) \cdot \mathbf{n}_{i,j}^k$ is the semi discrete relative vorticity. Note that (19-20) is a non linear dynamical system. It is expected to be fourth order accurate in $\Delta = \Delta\xi = \Delta\eta$. There is no upwinding in the spatial approximation. As a consequence, the accuracy of the discrete equilibrium solutions are 4-th order as well. In particular, the discrete equilibrium is not perturbed by the upwinding of the flux function as in finite volume methods¹. Refer to Section 3.5.1 for a numerical example with the SW equations. As we shall see in

¹This perturbation requires the so-called well-balanced correction

the numerical results, there is no need for any additional numerical viscosity in space. In fact, the intrinsic numerical viscosity of the RK4 scheme in Algorithm 2 presented in Section 2.5 is sufficient for stability in most situations.

2.5. Time stepping scheme with filtering. The time discretization is based on the classical Runge-Kutta order 4 scheme to which a filtering operation is added at each time iteration. The time discretization is given by the Algorithm 2.

Algorithm 2 : Explicit Runge-Kutta Scheme of order 4 with filter

```

1:  $q^0 = q^{(0)}$  given
2: for  $n = 0, 1, \dots$  do
3:    $K^{(1)} = J_{\Delta}(q^n)$ ,
4:    $K^{(2)} = J_{\Delta}\left(q^n + \frac{\Delta t}{2}K^{(1)}\right)$ ,
5:    $K^{(3)} = J_{\Delta}\left(q^n + \frac{\Delta t}{2}K^{(2)}\right)$ ,
6:    $K^{(4)} = J_{\Delta}\left(q^n + \Delta t K^{(3)}\right)$ ,
7:    $q^{n+1} = \mathcal{F}\left(q^n + \frac{\Delta t}{6}\left(K^{(1)} + 2K^{(2)} + 2K^{(3)} + K^{(4)}\right)\right)$ .
8: end for
    
```

In line 7 of Algorithm 2, \mathcal{F} denotes the so-called *filtering function*. This filtering step eliminates the +1/-1 mode attached to the grid and improves the stability properties (see Section 4). On the Cubed-Sphere, we use a filter of the form

$$(21) \quad \mathcal{F} = \frac{1}{2} (\mathcal{F}_{\xi} \circ \mathcal{F}_{\eta} + \mathcal{F}_{\eta} \circ \mathcal{F}_{\xi}).$$

The functions \mathcal{F}_{ξ} and \mathcal{F}_{η} correspond to a 10-th order filter in the directions ξ and η respectively. We refer to (95), (96) and the last line in Table 2 for the 10-th order filter function which is used. We let operate the filter function \mathcal{F}_{ξ} along the great circles in a fashion similar to the operator δ_{ξ}^H . The same steps than in Algorithm 1 are used. As in Algorithm 1, the data are completed by an interpolation procedure in the panels (II) and (IV). The difference between \mathcal{F} and δ_{ξ}^H is that the operator \mathcal{F}_{ξ} is explicit with a non compact stencil.

Several variants of compact formulas, of filter functions and of interpolation in the interpolation step of Algorithm 1 have been tested. There is no evidence of better behaviour or accuracy with alternative choices. Furthermore, the 10th order filter function in the last line of Table 2 is a good compromise between accuracy and stability.

3. NUMERICAL RESULTS

In this section, we present numerical results obtained with our centered compact scheme. We begin by showing results on the accuracy of the discrete divergence and vorticity (13) on particular exemples. Refer also to [10, 11].

From Section 3.3 on, we consider the hyperbolic problems (1), (2) and (3). In the three cases, the basic scheme relies on the same principle. First the equations are discretized in space. This gives a system of the form (19) by applying the discrete space operators pointwise. Second, the semi-discrete system is discretized in time by the Algorithm 2.

Consider a non zero function $f(\mathbf{x})$ defined on \mathbb{S}_a with restriction to the grid $(f^*)_{i,j}^k = f(\mathbf{s}_{i,j}^k)$. The error e_p , $p = 1, 2, \infty$ between f^* and some approximant $\hat{f}_{i,j}^k$ is defined by

$$(22) \quad e_p = \frac{\|(f^*)_{i,j}^k - \hat{f}_{i,j}^k\|_p}{\|(f^*)_{i,j}^k\|_p}.$$

In (22), the norm $\|\cdot\|_p$ stands for

$$(23) \quad \|f_{i,j}^k\|_p = Q_N(|f|^p)^{1/p},$$

where $Q_N(f)$ denotes a quadrature rule on the Cubed Sphere with parameter N . We have used the rule (20) in [27], which is of the form

$$(24) \quad Q_N(f) = a^2 \sum_{k=(I)}^{(VI)} \sum_{i,j=-N/2}^{N/2} \alpha_{i,j} (f^*)_{i,j}^k,$$

We refer to [27]. for the definition of the weights $\alpha_{i,j}$.

Finally, note that the convergence analysis is performed by evaluating the least squares fit for several grids.

3.1. Steady state in a spherical cap. This test was suggested in [5]. Consider the scalar conservation law:

$$(25) \quad \frac{\partial u}{\partial t} + \operatorname{div}_T \mathbf{F}(x, u) = 0.$$

The sphere is \mathbb{S}_a with $a = 1$. The tangential field $\mathbf{F}(x, u)$ has the form

$$(26) \quad \mathbf{F}(x, u) = \begin{bmatrix} x \\ y \\ z \end{bmatrix} \times \begin{bmatrix} f_1(u) \\ f_2(u) \\ f_3(u) \end{bmatrix}.$$

with

$$(27) \quad f_1(u) = f_2(u) = f_3(u) = \frac{1}{2}u^2.$$

The function

$$(28) \quad u_0(x, y, z) = (x + y + z)/\sqrt{3}$$

is a time independent solution of (25). Thus it can be compared at any time to the numerical solution. This enables to assess the accuracy of the approximate divergence in a nonlinear context. Fig. 5 reports at time $T = 6$ the relative errors e_p , $p = 1, 2, \infty$ and the integral of u on the sphere, which must remain constant as time evolves. Fig. 6 reports the same quantities but at time $T = 600$. In both cases, a coarse grid $32 \times 32 \times 6$, is used with $\Delta t = \frac{0.96}{\pi} \Delta \xi$. The growth remains bounded by small values in both cases, even at $T = 600$. Finally, Fig 7 reports the convergence rate at time $T = 6$ using several grids. A convergence rate close to 4 is observed in all norms.

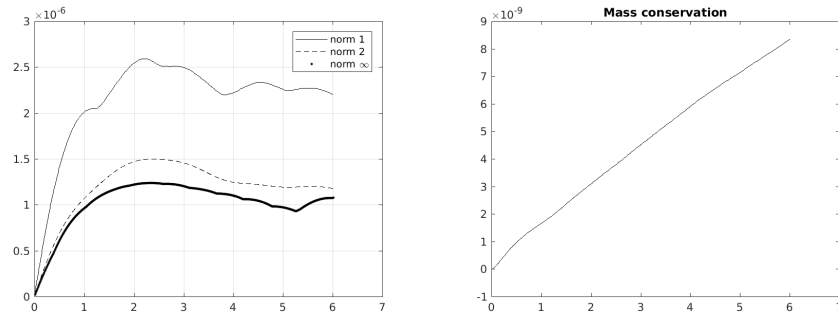
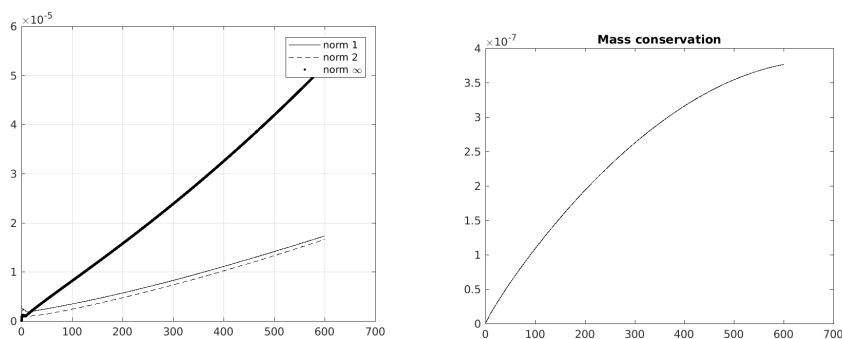
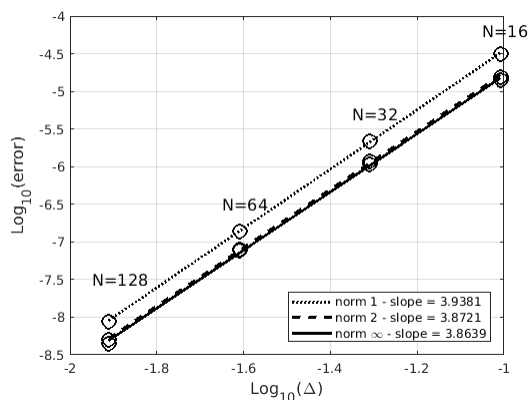


FIGURE 5. Spherical cap test case: comparison between the time independent exact solution $u_0(x, y, z) = (x + y + z)/\sqrt{3}$ and the approximate solution $u_{i,j}^k(t)$ for the conservation law (25). Left panel: error history $e_p(t) = \|(u_0^*)_{i,j}^k - u_{i,j}^k(t)\|_p / \|(u_0^*)_{i,j}^k\|_p$ with $p = 1, 2, \infty$ for $0 \leq t \leq T = 6$. Right panel: conservation of the integral of $u(t, x)$ on the sphere.


 FIGURE 6. Same as Fig. 5 but on the time interval $0 \leq t \leq T = 600$.

 FIGURE 7. Spherical cap test case: convergence for the steady state of (25). The error at time $T = 6$ is reported. The convergence rate is close to 4 in all norms.

3.2. Accuracy of the approximate relative vorticity. Consider a tangential vector field \mathbf{v} . The *relative vorticity* is the scalar defined by

$$(29) \quad \text{curl}_T(\mathbf{v}) = (\nabla_T \times \mathbf{v}) \cdot \mathbf{n}.$$

A natural approximation is

$$(30) \quad \text{curl}_{T,\Delta}(\mathbf{v}_{i,j}^k) = (\nabla_{T,\Delta} \times \mathbf{v}_{i,j}^k) \cdot \mathbf{n}(\mathbf{x}_{i,j}^k),$$

where the operator $\nabla_{T,\Delta} \times \mathbf{v}_{i,j}^k$ is defined in (13)_b. The accuracy of (30) is assessed with the two following tests, performed using functions defined on the spherical earth \mathbb{S}_a , with $a = 6.37122 \times 10^6$ m (earth radius).

(1) The first test consists in assessing numerically the identity

$$(31) \quad \text{curl}_T(\nabla_T h) = 0.$$

We consider the particular case of the function $h(\mathbf{x})$ defined on \mathbb{S}_a by

$$(32) \quad h(\lambda, \theta) = \cos^5(\theta) \sin(30\lambda),$$

with (λ, θ) the longitudinal and latitudinal coordinates. The observed convergence rate in the norm $\|\cdot\|_p / |\mathbb{S}_a|^{1/p}$ reported in Fig. 8 is close to 4.

(2) The second case represents a zonal wind with velocity

$$(33) \quad \mathbf{v}(\mathbf{x}) = \cos^\alpha(\theta) \mathbf{e}_\lambda(\mathbf{x}).$$

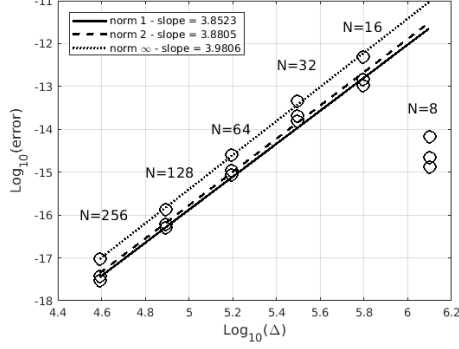


FIGURE 8. Accuracy of the identity $\text{curl}_T(\nabla_T h) = 0$, with test case (31) and the function $h(\lambda, \theta) = \cos^5(\theta) \sin(30\lambda)$. The errors $\|\cdot\|_p$ (normalized with $|\mathbb{S}_a|^{1/p}$) are reported with $p = 1, 2$ and ∞ . The grid $N = 8$ is too coarse to represent the function h .

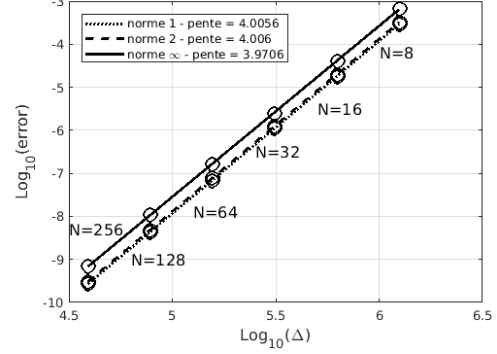


FIGURE 9. Accuracy of the relative vorticity (30) for the tangential field $\mathbf{v}(\mathbf{x}) = \cos^3(\theta)\mathbf{e}_\lambda(\mathbf{x})$. Convergence rate of the approximate relative vorticity of (33) for e_p with $p = 1, 2$ and ∞ with the same grid parameter than in Fig. 8.

The relative vorticity is

$$(34) \quad \text{curl}_T(\mathbf{v})(\mathbf{x}) = \frac{\alpha + 1}{a} \cos^{\alpha-1}(\theta) \sin(\theta).$$

Picking the parameter $\alpha \geq 2$ ensures that the field and the relative vorticity are regular near the poles. We have chosen in our test $\alpha = 3$. The relative error (22) is reported in Table 1 and in Fig. 9. A sharp 4th. order accuracy is observed in all norms.

N	e_1	e_2	e_∞
8	2.9158(-4)	3.3039(-4)	6.7103(-4)
16	1.7719(-5)	1.9906(-5)	4.0648(-5)
32	1.1025(-6)	1.2416(-6)	2.5207(-5)
64	6.9056(-8)	7.7821(-8)	1.6433(-7)
128	4.3244(-9)	4.8755(-9)	1.0822(-8)
256	2.7061(-10)	3.0522(-10)	6.9474(-10)
Rate	4.01	4.01	3.97

TABLE 1. Accuracy of the relative vorticity $\text{curl}_{T,\Delta}(\mathbf{v})$ for the tangential field $\mathbf{v}(\mathbf{x}) = \cos^\alpha(\theta)\mathbf{e}_\lambda(\mathbf{x})$. The relative error e_p given in (22) with $p = 1, 2, \infty$. A sharp 4-th order accuracy is observed in all norms.

3.3. Deformational flow with vortices. We consider the convection equation

$$(35) \quad \frac{\partial h}{\partial t}(t, \mathbf{x}) + \mathbf{c}(t, \mathbf{x}) \cdot \nabla_T h(t, \mathbf{x}) = 0$$

The velocity $\mathbf{c}(t, \mathbf{x})$ is prescribed to let evolve the initial condition with two constant states on a half sphere into a rollup structure. This structure consists of two vortices localised at two diametrally opposite points C and C' . As time evolves, filaments spiral around the two vortex centers. This behaviour is well known in point vortex flows. This test was introduced in [24, 28] as a sequel of the solid body test case (test 1) in [38].

Here the analytical solution is available by the characteristics method. This case is challenging to evaluate the spatial accuracy, since the filaments go below the resolution of the grid at some time. The time stepping accuracy is also evaluated. Two variants were introduced in [24, 28]. In the first variant, the velocity \mathbf{c} is time independent. It is given in the coordinate system (λ', θ') attached to the axis (CC') by

$$(36) \quad \mathbf{c}(\mathbf{x}) = a c_{\lambda'}(\mathbf{x}) \mathbf{e}_{\lambda'}(\mathbf{x}),$$

where

$$(37) \quad c_{\lambda'} = \cos(\theta') \omega_r(\theta'), \quad \omega_r(\theta') = \begin{cases} V(\theta')/(a\rho(\theta')) & \text{if } \rho \neq 0, \\ 0 & \text{if } \rho = 0. \end{cases}$$

and

$$(38) \quad \begin{cases} \rho(\theta') = \rho_0 \cos(\theta'), \\ V(\theta') = u_0 \frac{3\sqrt{3}}{2} \operatorname{sech}^2(\rho(\theta')) \tanh(\rho(\theta')). \end{cases}$$

with parameters $T > 0$, $\rho_0 > 0$ and $u_0 = 2\pi a/T$. The solution $h(t, \mathbf{x})$ is given in coordinates (λ', θ') by

$$(39) \quad h(t, \lambda', \theta') = 1 - \tanh\left(\frac{\rho(\theta')}{\gamma} \sin(\lambda' - \omega_r(\theta')t)\right),$$

The values $\rho_0 = 3$, $\gamma = 5$, $T = 12$ days (in seconds) and earth radius $a = 6.37122 \times 10^6$ m. Fig. 10 reports the error history when the point C is at $(\lambda_C, \theta_C) = (\pi/4, \pi/4)$. It corresponds to a location of the vortices at the intersection of three panels. This test permits to assess the accuracy of the approximate gradient with Algorithm 1. The grid is fixed $36 \times 36 \times 6$. It is a coarse grid, with equatorial resolution $\Delta\lambda = 2.5$ deg. Two time steps were used to reach $T = 12$ days. In both cases, the scheme was found stable with a smoothly growing error. When performing 2880 iterations, the error is dominated by the spatial approximation. The observed error levels are comparable to the ones obtained with the Discontinuous Galerkin method in [28]. With 288 iterations, space and time errors are observed simultaneously, and the error level is slightly better in that case. Fig. 11 reports the convergence rate in the norms $p = 1$, $p = 2$ and $p = \infty$ with 205 iterations. The error convergence is of order greater than 4, which is better than expected.

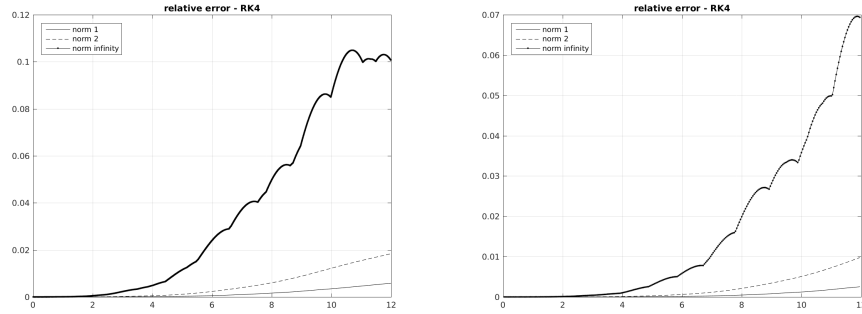


FIGURE 10. Deformational test case, time independent velocity, [24, 28]. The axis (CC') is such that $(\lambda_C, \theta_C) = (\pi/4, \pi/4)$. Grid $36 \times 36 \times 6$. Left panel: error history with 2880 iterations. Right panel: error history with 288 iterations.

The second variant [28] consists in superposing to the preceding velocity a solid body rotation at constant speed. As a result, the rollup behaviour of the two antipodal vortices is now superposed to the traveling wave effect at constant speed. This makes the test more difficult for large time than the previous one. The velocity $\mathbf{c}(t, \mathbf{x})$ in (35) is $\mathbf{c}(t, \mathbf{x}) = \mathbf{c}_s(\mathbf{x}) + \mathbf{c}_r(t, \mathbf{x})$ where \mathbf{c}_r is the "static" velocity in (36) and \mathbf{c}_s is the solid rotation velocity defined by

$$(40) \quad \mathbf{c}_s(\mathbf{x}) = c_{\lambda,s}(\mathbf{x}) \mathbf{e}_\lambda(\mathbf{x}) + c_{\theta,s}(\mathbf{x}) \mathbf{e}_\theta(\mathbf{x})$$

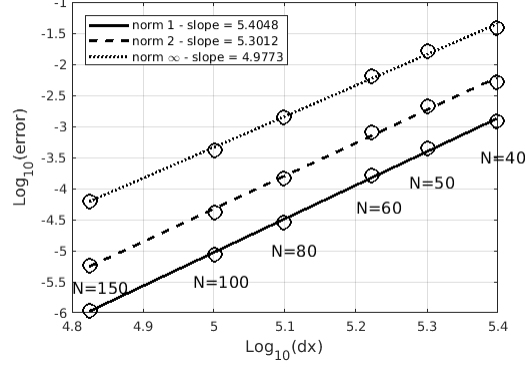


FIGURE 11. Deformational test case, time independent velocity (36). Convergence analysis at day 12. $(\lambda_C, \theta_C) = (\pi/4, \pi/4)$. With the grid $N \times N \times 6$, the time step is such that $\frac{2\pi u_0 \Delta t}{N} = 0.9$. The accuracy is close to 5.

with

$$(41) \quad \begin{cases} c_{\lambda,s} = u_0(\cos \theta \cos \alpha + \sin \theta \cos \lambda \sin \alpha), \\ c_{\theta,s} = -u_0 \sin \lambda \sin \alpha. \end{cases}$$

The parameters are the rotation angle α and $u_0 = 2\pi a/(12\text{days})$. In (39) the point C is now moving along solid body rotation. Its coordinates $(\lambda'_C(t), \theta'_C(t))$ are

$$(42) \quad (\lambda'_C(t), \theta'_C(t)) = (\lambda_0 + \omega_s t, \theta_0),$$

where $(\lambda_0, \theta_0) = (3\pi/2, 0)$ is the initial position of the vortex. The "static" velocity $\mathbf{c}_s(t, \mathbf{x})$ is

$$(43) \quad \mathbf{c}_r(t, \mathbf{x}) = c_{\lambda,r}(t, \mathbf{x})\mathbf{e}_\lambda(\mathbf{x}) + c_{\theta,r}(t, \mathbf{x})\mathbf{e}_\theta(\mathbf{x})$$

with

$$(44) \quad \begin{cases} c_{\lambda,r}(t) = a\omega_r \left[\sin \theta_C(t) \cos \theta - \cos \theta_C(t) \cos(\lambda - \lambda_C(t)) \sin \theta \right], \\ c_{\theta,r}(t) = -a\omega_r \cos \theta_C(t) \sin(\lambda - \lambda_C(t)). \end{cases}$$

where $\omega_r = u_0/a = 2\pi/(12\text{days})$ and $(\lambda_C(t), \theta_C(t))$ is the coordinates of the moving point C .

At $T = 12$ days, the error level is comparable to the Discontinuous Galerkin approximation in [28]. We also compare the results using two upwind finite volume schemes with high order reconstruction [20]. These two schemes are referred to as WENO5 and KL4 respectively. We have used the parameter $\alpha = \pi/4$. The grid is $80 \times 80 \times 6$ and 750 times iterations are performed (at $T = 12$ days). Typical results reported [20] with the WENO5 scheme give errors of $e_1 = 0.0021$, $e_2 = 0.0042$ and $e_\infty = 0.0191$. Using the KL4 scheme, errors are reported as $e_1 = 0.0021$, $e_2 = 0.0043$ and $e_\infty = 0.0194$. With the present scheme, using the parameters above, the observed errors are $e_1 = 1.67(-4)$, $e_2 = 7.23(-4)$ and $e_\infty = 5.75(-3)$ which is slightly better. In Fig. 12 a slice of the vortex after 12 days is represented with resolution $N = 30$ and $N = 60$, respectively. With a resolution $N = 60$, an excellent match with the exact solution is observed. Table 13 reports fourth order at final time.

Finally, we report in Fig. 14 the relative error history during a larger time of $T = 24$ days. This permits to observe the potential of the scheme at a time where a lack of accuracy is expected. We have used first a coarse grid $40 \times 40 \times 6$ with 457 time iterations and second a fine grid $80 \times 80 \times 6$ with 914 time iterations. With the coarse grid, the error level after 24 days is 15.93% in the maximum norm and 3.67% in the L^2 norms. With the fine grid, the errors is below 9.63% for the maximum norm and 1.69% with the L^2 norms.

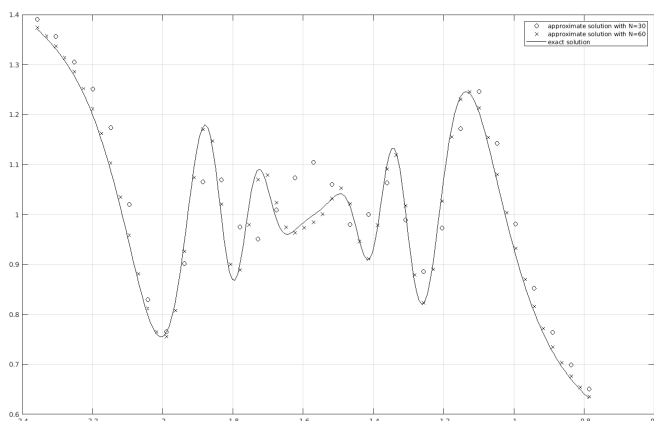


FIGURE 12. Deformational test case, time dependent velocity (43). Slice of the vortex after 12 days: the value of h in (35) is displayed in function of the longitude angle (in radians). Solid line: exact solution. Circles: approximate solution with the grid $30 \times 30 \times 6$. Crosses: approximate solution with the grid $60 \times 60 \times 6$.

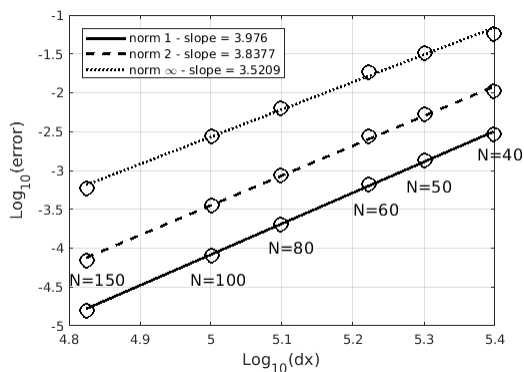


FIGURE 13. Deformational test case, time dependent velocity (43). The time step is given by $2\pi u_0 \Delta t / N = 0.7$ with $u_0 = 2\pi a / 1212 \text{ days}$, the earth radius a and $\alpha = \pi/4$. Convergence slope at final time in the three norms e_p , $p = 1, 2, \infty$.

3.4. Linearized shallow water equation. We consider the shallow water equation (2) linearized around an atmosphere at rest. We consider two cases designed using hand manufactured solutions. The source terms S_η and S_v are adjusted to these solutions. The numerical scheme uses the approximation (9 - 13) with the filtered RK4 scheme (Algorithm 2). As before, the approximation in space is centered.

The first test case serves to assess the accuracy of the approximate gradient and divergence (9) and (13) when used in the LSWE system (2). Consider the two exponentially in time damped functions

$$(45) \quad \begin{cases} \tilde{\eta}(t, \mathbf{x}) &= \varphi(\theta) e^{-\sigma t}, \\ \tilde{\mathbf{v}}(t, \mathbf{x}) &= \frac{\sqrt{gH}}{10} \varphi(\theta) e^{-\sigma t} \mathbf{e}_\lambda(\mathbf{x}). \end{cases}$$

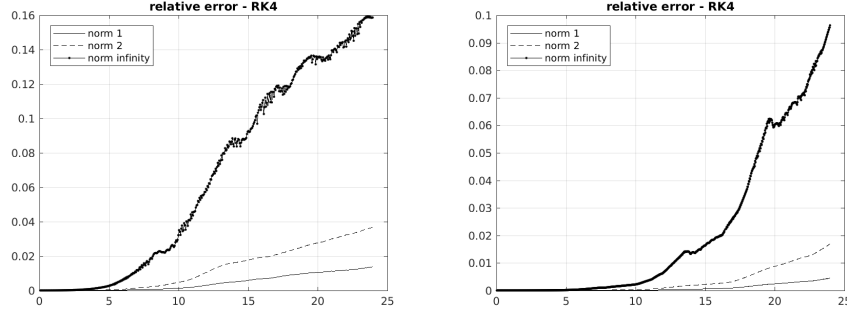


FIGURE 14. Deformational test case, time independent velocity [28]. The angle parameter is $\alpha = \pi/4$. The error history of the relative error is reported for 24 days. Left panel: grid $40 \times 40 \times 6$ and 457 time iterations. The relative error levels are after 24 days: L^1 norm: 1.36%, L^2 norm: 3.67%, L^∞ norm: 15.93%, Right panel: grid resolution $80 \times 80 \times 6$ and 914 time iterations. The relative error levels are after 24 days: L^1 norm: 0.45%, L^2 norm: 1.69%, L^∞ norm: 9.63%,

with

$$(46) \quad \varphi(\theta) = \begin{cases} 0 & \text{if } \theta \leq \theta_0, [10pt] \\ \frac{1}{e_n} \exp \left[\frac{1}{(\theta - \theta_0)(\theta - \theta_1)} \right] & \text{if } \theta_0 \leq \theta \leq \theta_1, [10pt] \\ 0 & \text{if } \theta_1 \leq \theta. \end{cases}$$

The normalization constant $e_n = \exp \left[\frac{-4}{(\theta_0 - \theta_1)^2} \right]$ gives $\varphi(\theta_0) = \varphi(\theta_1) = 1$.

We have picked $\sigma = 10^{-5}$, $\theta_0 = -\pi/3$, $\theta_1 = \pi/3$. The system to be solved is (2) where the source terms S_η and S_v are defined such that $(\tilde{\eta}(t, \mathbf{x}), \tilde{v}(t, \mathbf{x}))^T$ is solution. In Fig. 15, left panel, the least squares slope is reported using three grids.

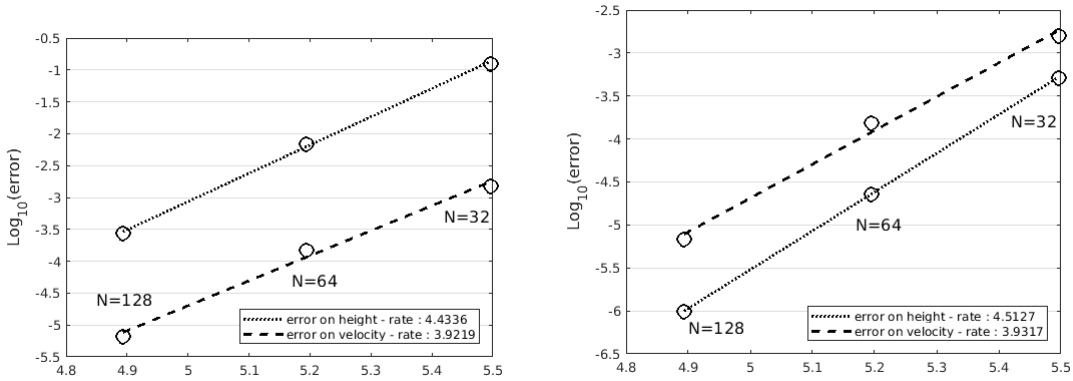


FIGURE 15. Convergence of the compact scheme in the case of the LSWE equations (2). Left panel: the Hermitian scheme applied to the exponential decaying solution (45) of the LSWE. The source term S_η and S_v are adjusted to the decaying solution (45). The final time is 1.5 hour and $H = 10^5$ meters. Right panel: time independent zonal solution (47) and (48) of the LSWE system. The slope is very close in the two cases. The observed error level is better in the time independent case.

The second case is a time independent zonal solution. To a parameter function $\varphi(\theta)$ given by (46) corresponds the velocity $\mathbf{v}(\mathbf{x})$ defined by

$$(47) \quad \mathbf{v}(\mathbf{x}) = u_0 \varphi(\theta) \mathbf{e}_\lambda(\theta).$$

Integrating the momentum equation (2)₂ gives

$$(48) \quad \eta(\mathbf{x}) = \eta_{eq} - \frac{a \cdot u_0}{g} \int_0^\theta f(s) \varphi(s) ds.$$

The functions (47) and (48) are a zonal divergence free solution of (LSWE). This test case serves to assess the accuracy of the approximation in space. In particular, the accuracy of the zero divergence preserving for large time. The numerical results are reported in the right panel in Fig. 15.

3.5. Shallow Water equations. Numerical results are displayed on four standard test cases involving the (SW) system (3). As in Sections 3.3 and 3.4 we use the scheme (19). The differential operators gradient, divergence and vorticity are discretized directly without any upwinding by (9-13). The time scheme is given in Algorithm 2. First, the cases 2, 5 and 6 from the standard suite [38] are considered. They are referred to as the geostrophic steady-state flow, the isolated mountain case and the Rossby-Haurwitz case. The fourth case is the barotropic instability case of Galewsky *et al.* [13]. In all cases the results are compared to the literature. As we shall see, the compact scheme behaves very well in all cases. The conservation properties of the scheme are also numerically analyzed. The constants are $a = 6.37122 \times 10^6 \text{m}$ (earth radius), $\Omega = 7.292 \times 10^{-5} \text{s}^{-1}$ (earth angular velocity), and $g = 9.80616 \text{m s}^{-2}$ (gravity constant). The Coriolis force is $f(\mathbf{x}) = 2\Omega \sin \theta$.

The following averaged values are preserved at the continuous level.

- mass : $I_1 = \int_{\mathbb{S}_a^2} h^* ds$,
- energy : $I_2 = \int_{\mathbb{S}_a^2} \frac{1}{2} h^* \mathbf{v}^2 + \frac{1}{2} g (h^2 - h_s^2) ds$,
- potential enstrophy : $I_3 = \int_{\mathbb{S}_a^2} \frac{(\zeta + f)^2}{2h^*} ds$ with ζ the relative vorticity,
- divergence : $I_4 = \frac{1}{|\mathbb{S}_a|} \int_{\mathbb{S}_a^2} \nabla_T \cdot \mathbf{v} ds$,
- relative vorticity: $I_5 = \frac{1}{|\mathbb{S}_a|} \int_{\mathbb{S}_a^2} (\nabla_T \times \mathbf{v}) \cdot \mathbf{n} ds$.

The numerical error for I_1 , I_2 and I_3 is reported using the relative (algebraic) value

$$(49) \quad \frac{I_p(t) - I_p(0)}{I_p(0)}, p = 1, 2, 3.$$

In the two last cases, the value of I_4 and I_5 is reported. In all cases, the numerical integrals are calculated by (24).

3.5.1. Time-independent geostrophic flow. The test case 2 in [38] consists in assessing the accuracy in space of the scheme for a zonal time independent solution of (3). The angle α is a parameter representing the angle of an axis with the Oz direction. This parameter serves to observe the influence of the position of the grid with respect to the zonal equilibrium solution. In our case, it permits to evaluate how the Cubed Sphere operates with an oblique orientation. The Coriolis force is expressed as

$$(50) \quad f(\mathbf{x}) = 2\Omega (-\cos \lambda \cos \theta \sin \alpha + \sin \theta \cos \alpha).$$

The exact solution is (h, \mathbf{v}) , with $\mathbf{v} = u \mathbf{e}_\lambda + v \mathbf{e}_\theta$:

$$(51) \quad \begin{cases} h &= h_0 - \frac{1}{g} \left(a\Omega u_0 + \frac{u_0^2}{2} \right) (-\cos \lambda \cos \theta \sin \alpha + \sin \theta \cos \alpha)^2, \\ u &= u_0 (\cos \theta \cos \alpha + \cos \lambda \sin \theta \sin \alpha), \\ v &= -u_0 \sin \lambda \sin \alpha. \end{cases}$$

The constants gh_0 is $gh_0 = 2.94 \times 10^4 \text{m}^2 \text{s}^2$ and $u_0 = 2\pi a / (12 \text{days})$ (in ms^{-1}). Fig. 16 shows the history of the relative error on h in the case $\alpha = \pi/4$. Error growths are monotonic and very slow. Fig. 17 reports the convergence slope for h . In both cases ($\alpha = 0$ and $\alpha = 45$), a sharp 4-th order accuracy is obtained. The error e_∞ at day 5 is close to $2.78 \cdot 10^{-6}$ to be compared with $5.86 \cdot 10^{-6}$ in [7] (Table 5), where a fourth order finite volume scheme is used. In [35], the reported error is $1.47 \cdot 10^{-6}$ (extrapolated for $N=32$) also with a fourth order finite volume scheme using the AUSM+ numerical flux function. The numerical evaluation of

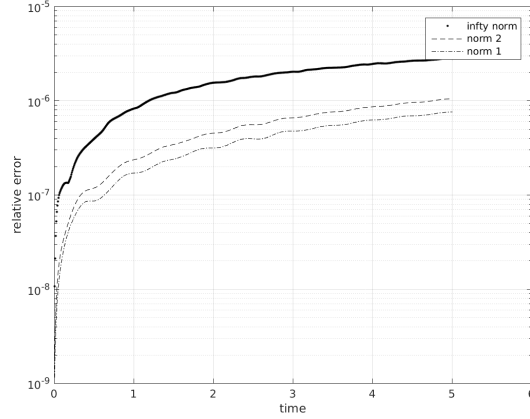


FIGURE 16. Steady state geostrophic flow with $\alpha = \pi/4$ on a Cubed Sphere with $N = 32$ after 5 days. The relative error e_p with $p = 1, 2, \infty$ is plotted. The time step is 605.85s for the grid $32 \times 32 \times 6$, 302.93s for the grid $64 \times 64 \times 6$ and 151.46s for the grid $128 \times 128 \times 6$. The error e_∞ at day 5 is $2 \cdot 10^{-6}$.

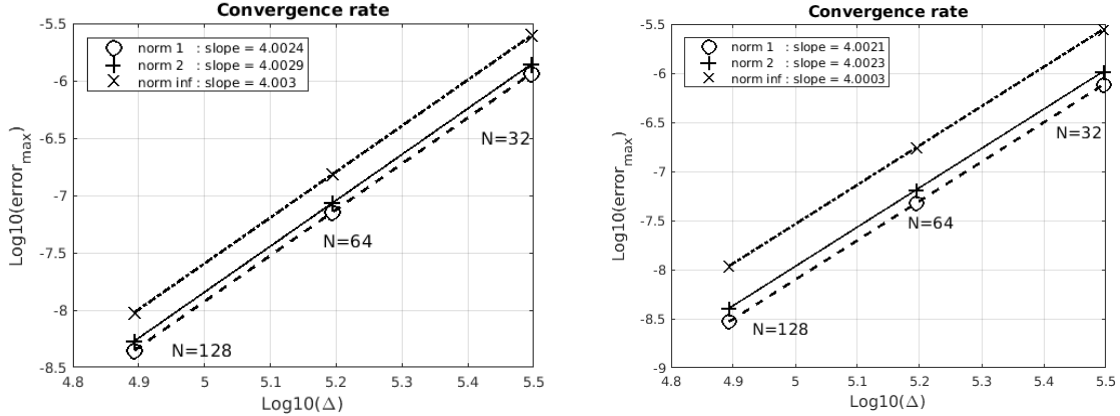


FIGURE 17. Steady state geostrophic flow at day 5. The time step is 605.85 s. Convergence slope of the relative error e_p on the total height h . Left panel: $\alpha = 0$. Right panel: $\alpha = \pi/4$. A sharp 4-th order accuracy is observed. There is no visible influence of the angle α .

the conservation relations is shown on Fig. 18. As can be observed, the level of conservation error for $I_q(t)$, $q = 1, \dots, 5$ is very good.

3.5.2. *Isolated mountain test case.* The test case 5 in [38] is time dependent without analytical solution. The initial data consists of the time independent solution (51) with $h_0 = 5960\text{m}$, $u_0 = 20\text{m} \cdot \text{s}^{-1}$ and $\alpha = 0$. The

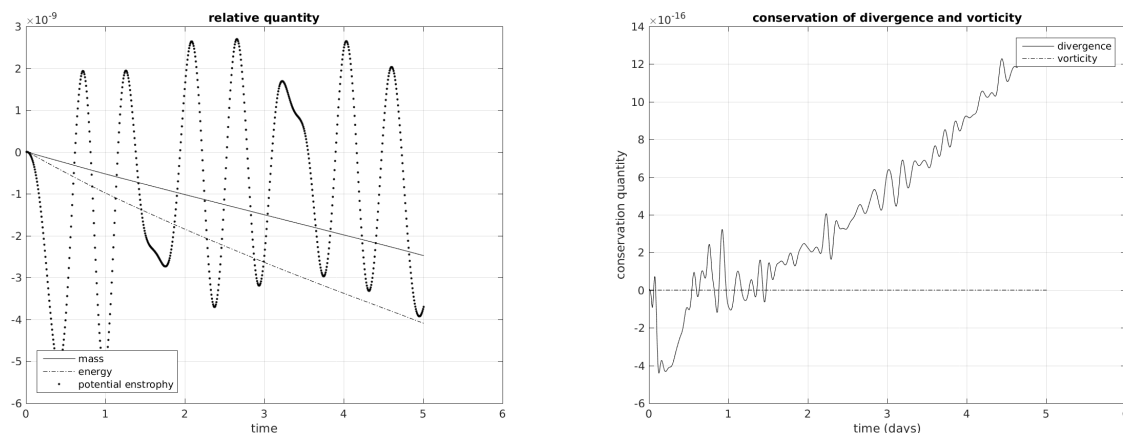


FIGURE 18. Steady state geostrophic flow with $\alpha = \pi/4$ with a grid $32 \times 32 \times 6$ after 5 days. The relative error $(I_p(t) - I_p(0))/I_p(0)$ is represented for the mass ($p = 1$), the energy ($p = 2$) and the potential enstrophy ($p = 3$). The time step is 605.85s with the grid $32 \times 32 \times 6$, 302.92s with the grid $64 \times 64 \times 6$ and 151.46s with the grid $128 \times 128 \times 6$. The value $I_p(t)$ is represented for the divergence ($p = 4$) and the relative vorticity ($p = 5$). In all cases, the error level shows very good numerical conservation.

function h^* in (3) is $h^* = h - h_s$ where h is the total height and h_s is the bottom topography. The function h_s (the "isolated mountain") is defined by

$$(52) \quad \begin{cases} h_s = h_{s_0} \left(1 - \frac{r}{r_0}\right), & h_{s_0} = 2000\text{m}, \\ r = \min\left(r_0, \sqrt{(\lambda - \lambda_c)^2 + (\theta - \theta_c)^2}\right), & r_0 = \pi/9, \quad (\lambda_c, \theta_c) = (3\pi/2, \pi/6). \end{cases}$$

The total height h is reported at days 5, 10 and 15 in Fig. 19 using a coarse Cubed Sphere with $N = 32$. The isolines are visually similar to the ones obtained with the fourth order finite volume schemes in [35, 7]. The conservation history for the approximate values I_p , $p = 1 \dots 5$ is represented in Fig. 20. At day 15, the error difference in potential enstrophy is around $-0.9 \cdot 10^{-4}$ ($N=32$), similar to $-1.0 \cdot 10^{-4}$ in [7]. This is slightly better than $-3.3 \cdot 10^{-4}$ ($N=40$) with the FV4 scheme (and AUSM+ flux) in [35]. Also, the behavior of the error history is similar to the one in [7]. In [35], the error behavior is more irregular.

3.5.3. Rossby-Haurwitz test case. The Rossby-Haurwitz case is considered, (test 6 in [38]). This test consists of the Rossby-Haurwitz case. This test consists in an analytical solution of the nonlinear barotropic vorticity equation [26] and not of the (SW) equations 3. However, it is of great importance for assessing the qualitative behaviour of any numerical method for the shallow water model on the sphere. The initial velocity is $\mathbf{v} = u \cdot \mathbf{e}_\lambda + v \cdot \mathbf{e}_\theta$ with:

$$(53) \quad \begin{cases} u &= a\omega \cos \theta + aK \cos^{R-1} \theta (R \sin^2 \theta - \cos^2 \theta) \cos R\lambda, \\ v &= -aKR \cos^{R-1} \theta \sin \theta \sin R\lambda. \end{cases}$$

The initial total height h is :

$$(54) \quad gh = gh_0 + a^2 A(\theta) + a^2 B(\theta) \cos R\lambda + a^2 C(\theta) \cos 2R\lambda.$$

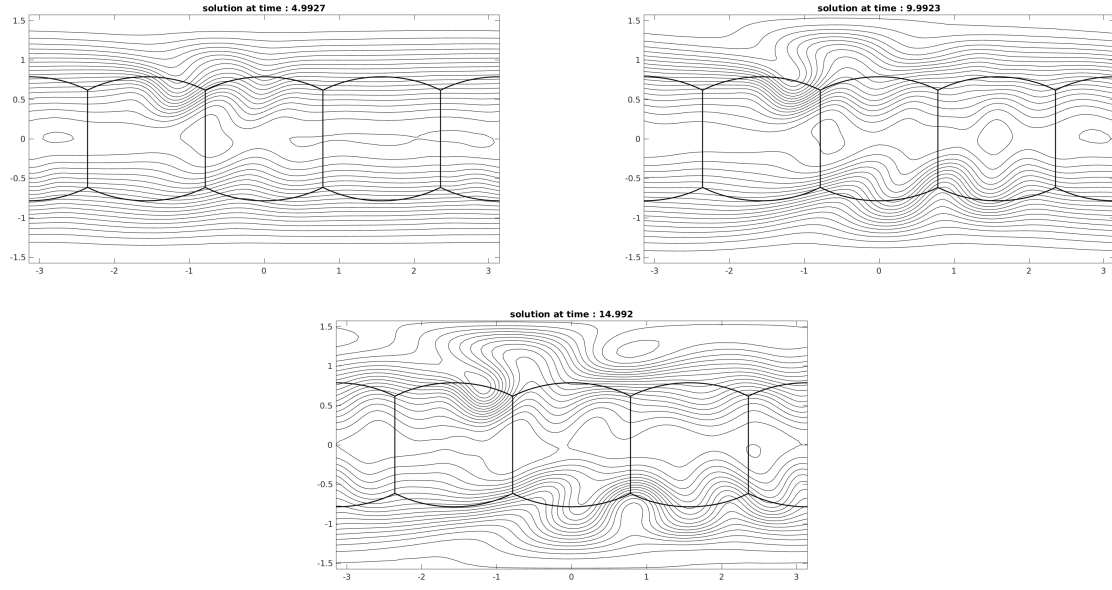


FIGURE 19. Isolated mountain test case at times of 5, 10 and 15 days. The total height h is represented. The Cubed Sphere $32 \times 32 \times 6$ is used. The contour line are plotted from 5050 m to 5950 m with interval of 50 m. The time step is 605.85 s. The results are similar to the literature.

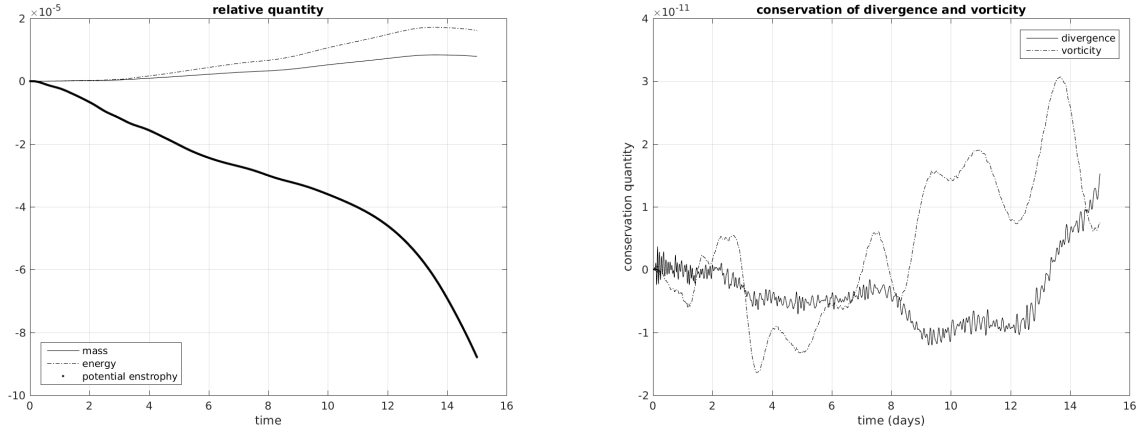


FIGURE 20. Isolated mountain test case with a grid $32 \times 32 \times 6$. The time step is 605.85 s. Left panel: History of the relative values $(I_q(t) - I_q(0))/I_q(0)$ for the mass ($q = 1$), total energy ($q = 2$) and potential enstrophy ($q = 3$). Right panel: Values of $I_q(t)$ for the divergence ($q = 4$) and the vorticity ($q = 5$).

with

$$(55) \quad \begin{cases} A(\theta) = \frac{\omega}{2} (2\Omega + \omega) \cos^2 \theta + \frac{1}{4} K^2 \cos^{2R} \theta [(R+1) \cos^2 \theta + (2R^2 - R - 2) - 2R^2 \cos^{-2} \theta], \\ B(\theta) = \frac{2(\Omega + \omega)K}{(R+1)(R+2)} \cos^R \theta [(R^2 + 2R + 2) - (R+1)^2 \cos^2 \theta], \\ C(\theta) = \frac{1}{4} K^2 \cos^{2R} \theta [(R+1) \cos^2 \theta - (R+2)]. \end{cases}$$

and with the constants $\omega = 7.848 \times 10^{-6} \text{s}^{-1}$, $K = 7.848 \times 10^{-6} \text{s}^{-1}$, $h_0 = 8 \times 10^3 \text{m}$ and $R = 4$. We report the total height h at days 7 and 14 in Fig. 21 and with a grid $80 \times 80 \times 6$. According to numerical experiments, a lower resolution is not sufficient with our scheme. This initial condition is well known to lead to an instable behaviour, associated to a turbulent pattern [34]. For this reason it is interesting to push in time the numerical scheme to observe the transition time. As reported in [35], the transition time is very sensitive to numerical parameters of the employed scheme, in particular to the amount of numerical dissipation. In [36], transition times are reported to vary from day 30 to beyond day 90. In our case, the approximation does not have parameters. The behaviour of the solution is reported in Fig. 22 with a $128 \times 128 \times 6$ grid at day 14, 28, 42 and 56. At that last time, the transition has already appeared.

Conservation history with the grid $128 \times 128 \times 6$ is reported in Fig. 23 for the first 14 days. Mass and energy relative errors are close to 10^{-9} . The level of the relative error on the enstrophy is around 10^{-3} . The error level on the divergence and the vorticity is observed to be around 10^{-13} . Finally, we report for completeness in Fig. 24 the same conservation history up to 80 days. A numerical breakdown can be indentified around day 50 on the divergence.

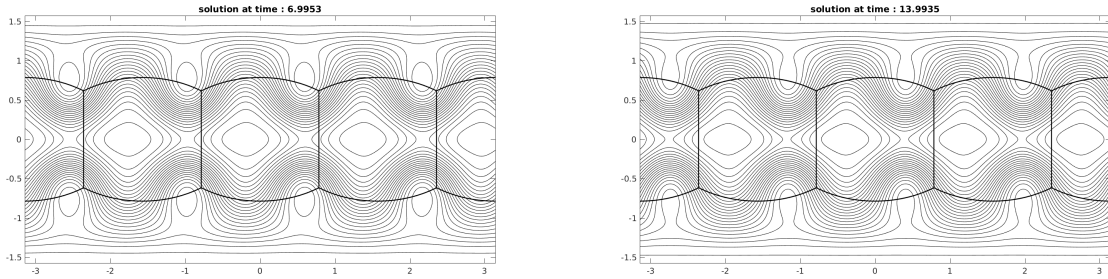


FIGURE 21. Numerical results of the Rossby-Haurwitz test case with the grid $80 \times 80 \times 6$. Left panel: day 7. Right panel: day 14. The time step is 242.34 s. Contour line are plotted from 8100 m to 10500 m with interval of 100 m.

3.5.4. *Barotropic instability.* Our last test is the barotropic instability test in [13]. The initial condition has the form $(h + h', \mathbf{v})$ where (h, \mathbf{v}) is a steady state zonal solution of (3). This steady state is given by :

$$(56) \quad \begin{cases} h(\lambda, \theta) = h_0 - \frac{1}{g} \int_{-\pi/2}^{\theta} a u_{\lambda}(\tau) \left(f + \frac{\tan(\tau)}{a} u_{\lambda}(\tau) \right) d\tau, \\ \mathbf{v} = u_{\max} \varphi(\theta) \mathbf{e}_{\lambda}. \end{cases}$$

where $\varphi(\theta)$ is given in (46) with $\vartheta_0 = \pi/7$, $\vartheta_1 = \pi/2 - \vartheta_0$. In addition, $u_{\max} = 80 \text{m s}^{-1}$, and h_0 is such that the mean value of h over \mathbb{S}_a be $h_0 = 10^4 \text{m}$. The perturbation h' added to h is

$$(57) \quad h'(\lambda, \theta) = \hat{h} \cos(\theta) \exp \left[- \left(\frac{\lambda}{\alpha} \right)^2 - \left(\frac{\theta_2 - \theta}{\beta} \right)^2 \right],$$

with $\hat{h} = 120 \text{m}$, $\alpha = 1/3$, $\beta = 1/15$ and $\theta_2 = \pi/4$. This test is reported as challenging for the Cubed-Sphere [32] due to the fact that the perturbation is located between panels (I) and (V), thus possibly giving rise to interpanel instabilities. In addition, the largest magnitude of ∇h is located near the boundary of panel (V).

In Fig. 25, contour lines of the vorticity are represented at day 6 for grids $64 \times 64 \times 6$, $96 \times 96 \times 6$ and $128 \times 128 \times 6$ respectively. The results are similar to those in [35, 7]. As mentioned in [35], the grid $32 \times 32 \times 6$ does not have enough spatial resolution to represent the initial data. The history of the conserved quantities is reported in Fig. 26 with the grid $128 \times 128 \times 6$. Again the relative potential vorticity is difficult to preserve, with a relative error at day 6 reaching $-2.5 \cdot 10^{-3}$. Note finally that even in this case, there is apparently no need of any upwinding to deal with the nonlinearity. The linear filtering combined with the inherent viscosity of the RK4 scheme is sufficient once again to obtain accurate results.

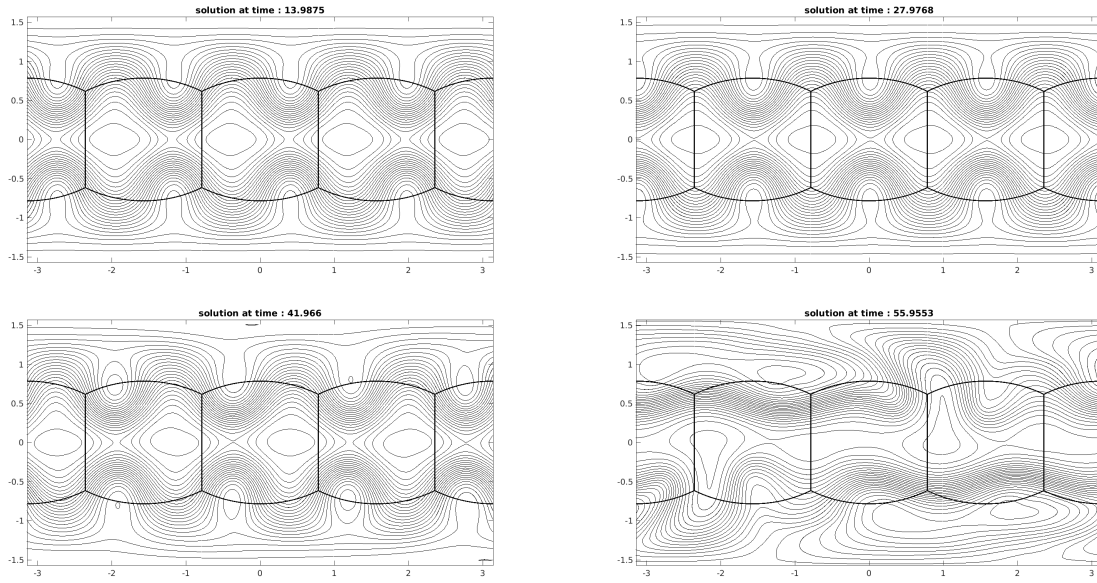


FIGURE 22. Numerical results of Rossby-Haurwitz wave test case with the Cubed Sphere $128 \times 128 \times 6$. From top right to bottom left: day 14, 28, 42 and 56. The time step is 151.46 s (31945 time iterations for 56 days). Contour lines are plotted from 8100 m to 10500 m with an interval of 100 m.

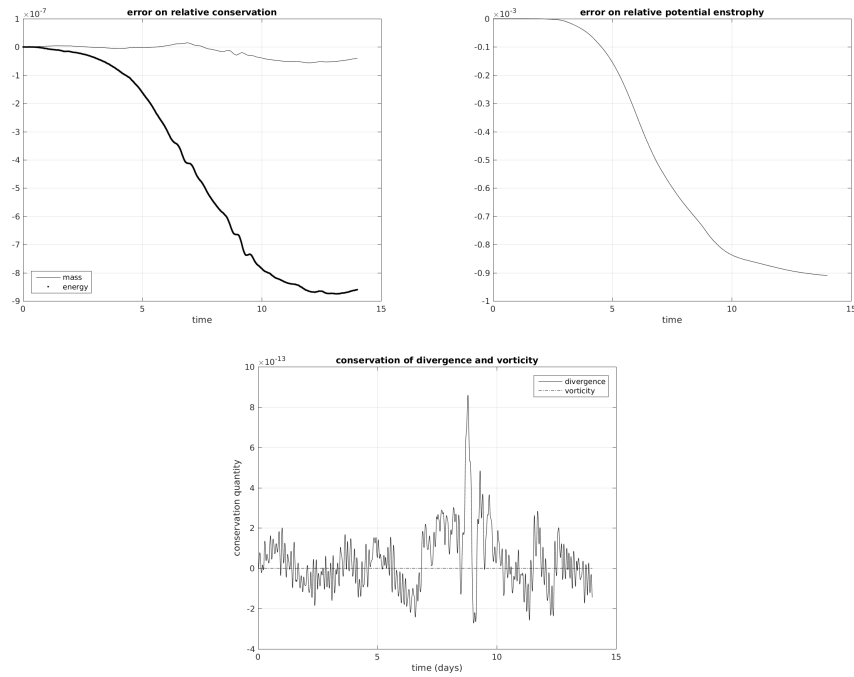


FIGURE 23. History of the conserved integrals $I_q(t)$ for the Rossby-Haurwitz wave test case with the grid $80 \times 80 \times 6$ (preferably $80 \times 80 \times 6$) with 14 days. The time step is 242.34 sec. Top left panel: mass and total energy. Top right panel: potential enstrophy. Bottom panel: divergence and vorticity. The relative error for the potential vorticity reaches 0.1%.

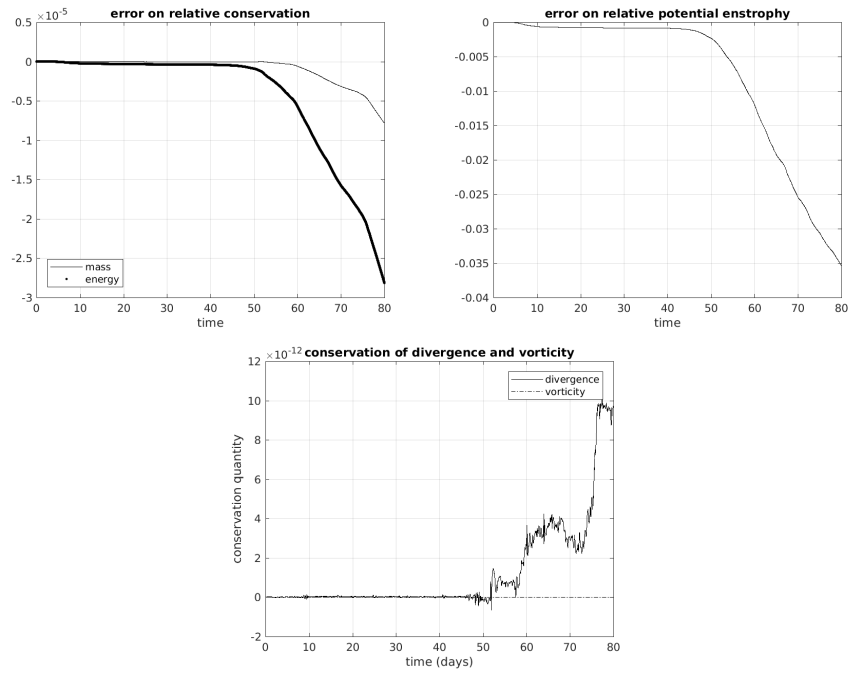


FIGURE 24. Rossby-Haurwitz test case, (test 6 in [38]). History of the conserved quantities during 80 days. Top left panel: mass and total energy. Top right panel: potential enstrophy. Bottom: divergence and vorticity. The grid is $128 \times 128 \times 6$ with 80 days. The time step is 151.46 sec. The relative error for the potential vorticity reaches 3.5%. A transition time can be observed on the divergence is around the threshold of 45/50 days.

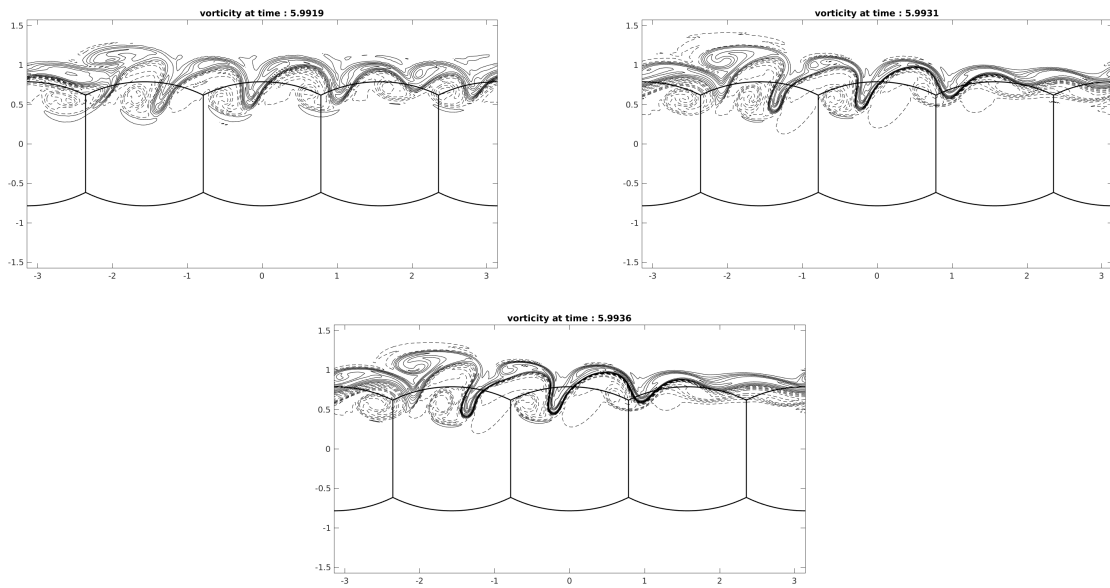


FIGURE 25. Barotropic instability test case. The numerical vorticity is represented at day 6 with the grids $64 \times 64 \times 6$, $\Delta t = 302.93$ s (top left), $96 \times 96 \times 6$, $\Delta t = 201.95$ s (top right), $128 \times 128 \times 6$, $\Delta t = 151.46$ s (bottom). The results show good consistency with the literature.

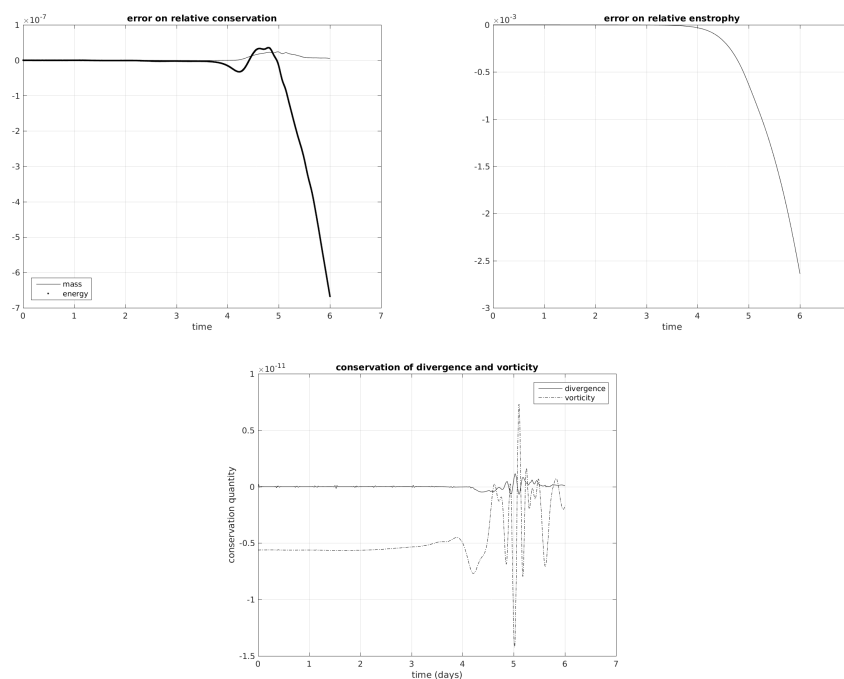


FIGURE 26. Barotropic instability test case with the grid $128 \times 128 \times 6$. History of conserved quantities during 6 days. Top left panel: mass and total energy. The time step is 151.46 sec. Top right panel: potential enstrophy. Bottom: divergence and vorticity.

4. NUMERICAL ANALYSIS

In this section, we gather several numerical analysis facts related to the approximation used in this study. The results are limited to the model problem of the linear convection equation in the periodic setting. Although purely linear and one dimensional, these results were hardly found in existing literature.

4.1. Convergence analysis. The approximation in space in Sections 2.3 and 2.4 is based on the standard Hermitian approximate derivative. Consider a regular finite difference grid with stepsize $h > 0$ and periodic data located at point $x_j = jh$, $j = 0, 1, \dots, N-1$. To any gridfunction $\mathbf{w} = [w_0, w_1, \dots, w_{N-1}]$, the Hermitian derivative $\delta_x^H \mathbf{w}$ is defined by

$$(58) \quad \delta_x \mathbf{w}_j - \sigma_x(\delta_x^H \mathbf{w})_j = 0, \quad 0 \leq j \leq N-1,$$

where the operators σ_x and δ_x are defined by

$$(59) \quad \sigma_x \mathbf{v}_j = \frac{1}{6} \mathbf{v}_{j-1} + \frac{2}{3} \mathbf{v}_j + \frac{1}{6} \mathbf{v}_{j+1}, \quad \delta_x \mathbf{v}_j = \frac{\mathbf{v}_{j+1} - \mathbf{v}_{j-1}}{2h}, \quad 0 \leq j \leq N-1.$$

It is well known that $\delta_x^H \mathbf{w}$ is a fourth order approximation to the derivative. A proof proceeds as follows. Suppose given a periodic function $u(x)$ with u^* the associated gridfunction defined by $u_j^* = u(x_j)$. For $\mathbf{w} = u^*$, $\delta_x^H u^*$ satisfies

$$(60) \quad \delta_x u_j^* - \sigma_x(\delta_x^H u^*)_j = 0, \quad 0 \leq j \leq N-1.$$

The truncation error for δ_x^H is evaluated using the Kernel Peano theorem for the Simpson quadrature formula [18, Chap. 7, pp. 282 sqq] as follows. Any regular function $u(x)$ satisfies

$$(61) \quad \delta_x u_j^* - \sigma_x(\delta_x u)_j^* = -\frac{1}{180} h^4 (\partial_x^{(5)} u)(\xi_j),$$

for some $\xi_j \in]x_{j-1}, x_{j+1}[$. The truncation error is

$$(62) \quad \tau_j = \delta_x^H u_j^* - (\partial_x u)_j^*.$$

Subtracting (58) from (61) gives that

$$(63) \quad \sigma_x \tau_j = -\frac{1}{180} h^4 (\partial_x^{(5)} u)(\xi_j).$$

The inverse of σ_x , considered as a bounded operator in the space of bounded periodic sequences equipped with the norm $\|\mathbf{w}\|_\infty = \max_j |w_j|$ satisfies the estimate [4]

$$(64) \quad \|\sigma_x^{-1}\|_\infty \leq 3.$$

Applying σ_x^{-1} to the gridfunction (63) gives the estimate of the truncation error τ :

$$(65) \quad \|\tau\|_\infty \leq \hat{C} h^4 \|\partial_x^{(5)} u^*\|_{\infty, (0, L)}, \quad \hat{C} = 1/60.$$

Next, consider the linear convection equation for the scalar function $u(t, x)$:

$$(66) \quad \partial_t u + c \partial_x u = 0, \quad x \in \Omega = (0, L), \quad t \geq 0, \quad c > 0,$$

with periodic conditions at $x = 0$ and $x = L$. The semidiscrete compact scheme is:

$$(67) \quad \frac{d}{dt} \mathbf{v}_j(t) + c \delta_x^H \mathbf{v}_j(t) = 0.$$

This scheme is a standard approximation for convection problems. Refer to [22, 16] and the references therein. Note that the total mass $h \sum_{j=0}^{N-1} \mathbf{v}_j(t)$ is constant in time, which expresses a conservation property of (67). An elementary convergence analysis, based on the energy method, for the scheme (67) is now carried out as follows. We denote the norm $|\mathbf{u}|_h$

$$(68) \quad |\mathbf{u}|_h = \left(h \sum_{j=0}^{N-1} |u_j|^2 \right)^{1/2}, \quad \|\mathbf{w}\|_{h, \infty} = \max_{0 \leq j \leq N-1} |w_j|.$$

The error $e_j(t) = u_j^*(t) - \mathbf{v}_j(t)$ evolves along the system

$$(69) \quad \frac{d}{dt} e_j(t) = c \left(\tau_j(t) - \delta_x^H e_j(t) \right), \quad 0 \leq j \leq N-1.$$

Taking the $(\cdot, \cdot)_h$ scalar product of (69) with $e(t)$ gives (the antisymmetry of δ_x^H is used):

$$(70) \quad 2 \left(\frac{d}{dt} e(t), e(t) \right)_h = 2c \left(\tau(t), e(t) \right)_h.$$

Let $\alpha > 0$ be a fixed parameter to be specified latter. The equation (70) implies

$$(71) \quad \frac{d}{dt} |e(t)|_h^2 \leq c \left(\alpha |\tau(t)|_h^2 + \frac{1}{\alpha} |e(t)|_h^2 \right).$$

Consider a positive regular function $f(t)$ defined on $[0, T]$. Gronwall's lemma states that assuming $f'(t) \leq Af(t) + B$ and $f(0) = 0$ with $A, B > 0$, then $f(t) \leq (B/A)(\exp(At) - 1)$ for $0 \leq t \leq T$. Using $f(t) = |e(t)|_h^2$, $A = c/\alpha$ and $B = c\alpha \max_{0 \leq t \leq T} |\tau(t)|_h^2$ yields the estimate

$$(72) \quad |e(t)|_h^2 \leq \alpha^2 (e^{ct/\alpha} - 1) \max_{0 \leq t \leq T} |\tau(t)|_h^2, \quad 0 \leq t \leq T.$$

On the other hand, the estimate (65) gives

$$(73) \quad \max_{0 \leq t \leq T} |\tau(t)|_h^2 \leq L \hat{C}^2 h^8 \|\partial_x^{(5)} u\|_{\infty, [0, T] \times [0, L]}^2.$$

This gives in (72)

$$(74) \quad |e(t)|_h^2 \leq \alpha^2 (e^{ct/\alpha} - 1) L \hat{C}^2 h^8 \|\partial_x^{(5)} u\|_{\infty, [0, T] \times [0, L]}^2, \quad 0 \leq t \leq T.$$

For t fixed, taking the minimum of the function $\alpha \mapsto \alpha^2 (e^{ct/\alpha} - 1)$ in (74) gives

$$(75) \quad |e(t)|_h^2 \leq \hat{C}^2 f_{\min} L c^2 t^2 h^8 \|\partial_x^{(5)} u\|_{\infty, [0, T] \times [0, L]}^2, \quad 0 \leq t \leq T.$$

where $f_{\min} = \min_{x>0} (x^2(e^{1/x} - 1))$. It is easily shown that $f_{\min} \leq 1.545$. Defining the constant $\tilde{C} = \hat{C}\sqrt{f_{\min}} \simeq 2.08 \cdot 10^{-2}$, we obtain finally the following

Proposition 4.1. Let $u_j^* = u(t, x)$ be the exact solution of (66) at points x_j and $\mathbf{v}_j(t)$ be the solution of semidiscrete scheme (67). The error $e_j(t) = u^*(t) - \mathbf{v}_j(t)$ satisfies the fourth order error estimate

$$(76) \quad |e_j(t)|_h \leq C(t) \|\partial_x^{(5)} u\|_{\infty, [0, T] \times [0, L]}, \quad 0 \leq t \leq T,$$

where $C(t) = \tilde{C}\sqrt{Lct}$ and $\tilde{C} \simeq 2.08 \cdot 10^{-2}$ is a universal constant.

The estimate (76) shows a linear evolution of the constant $C(t)$ in time from $t = 0$ to $t = T$.

Remark 4.2. The estimate (76) shows fourth order accuracy in the grid dependent norm $|\cdot|_h$. Note that the maximum norm estimate is more difficult to prove. Note also that the practical interest of Prop. 4.1 is limited to the constant velocity and regular grid cases.

4.2. Matrix stability analysis of the fully discrete scheme. In this section, we show how to derive analytically the matrix stability condition for (67) when discretized in time by the RK4 scheme. Let $V(t) = [v_0(t), v_1(t), \dots, v_{N-1}(t)]^T$. The equation (67) is equivalent to the vector equation

$$(77) \quad \begin{cases} \frac{d}{dt} V(t) = -\frac{c}{h} \mathbf{J} V(t), \\ V(0) = V_0 = [u_0^*, u_1^*, \dots, u_{N-1}^*]^T, \end{cases}$$

where \mathbf{J} is the $N \times N$ matrix defined by $(\mathbf{J}V)_j = \delta_x^H \mathbf{v}_j$. Let \mathbf{P} be the matrix of the left shift operator $u_j \mapsto u_{j-1}$ with N -periodic data.

$$(78) \quad \mathbf{P} = \underbrace{\begin{bmatrix} 0 & 1 & & & \\ & 0 & 1 & (0) & \\ & & \ddots & \ddots & \\ & (0) & & 0 & 1 \\ 1 & & & & 0 \end{bmatrix}}_{N \times N}.$$

The matrix \mathbf{J} is $\mathbf{J} = m(\mathbf{P})$ where

$$(79) \quad m(z) = \frac{1}{2} \frac{z - z^{-1}}{\frac{1}{6}(z + z^{-1}) + \frac{2}{3}}.$$

The matrices \mathbf{P} and \mathbf{J} are expressed as ²

$$(80) \quad \mathbf{P} = \sum_{k=-\frac{N}{2}+1}^{\frac{N}{2}} \omega^k R^k \otimes (R^k)^H,$$

and

$$(81) \quad \mathbf{J} = \sum_{k=-\frac{N}{2}+1}^{\frac{N}{2}} m(\omega^k) R^k \otimes (R^k)^H.$$

where $R^k = [R_0^k, R_1^k, \dots, R_{N-1}^k]^T \in \mathbb{C}^N$ is the vector with components

$$(82) \quad R_j^k = \frac{1}{\sqrt{N}} \omega^{kj}, \quad 0 \leq j \leq N-1, \quad \omega = \exp\left(\frac{2i\pi}{N}\right).$$

Using that $V(t) = \exp(-\frac{ct}{h} \mathbf{J}) V_0$ yields

$$(83) \quad V(t) = \sum_{k=-\frac{N}{2}+1}^{\frac{N}{2}} \exp\left(-\frac{c}{h} m(\omega^k) t\right) ((R^k)^H V_0) R^k.$$

²For X a $n \times m$ matrix, $X^H = \bar{X}^T$

Consider now the time stepping of (77) by the RK4 scheme, [17, Chap. IV.2, pp. 16-18]. Since the matrix $-c\mathbf{J}/h$ is constant, the RK4 time stepping coincides with the vector iteration

$$(84) \quad V^{n+1} = r(-\lambda\mathbf{J})V^n,$$

where $\lambda = c\Delta t/h > 0$ is the Courant number and $r(z)$ is the truncated exponential series

$$(85) \quad r(z) = 1 + z + \frac{z^2}{2!} + \frac{z^3}{3!} + \frac{z^4}{4!}.$$

Using (81) yields that V^n is

$$(86) \quad V^n = \sum_{k=-\frac{N}{2}+1}^{\frac{N}{2}} [r(-\lambda m(\omega^k))]^n ((R^k)^H V_0) R^k.$$

The sequence (86) is bounded if and only if

$$(87) \quad \max_{k=-N/2+1}^{N/2} |r(-\lambda m(\omega^k))| \leq 1.$$

This is equivalent to

$$(88) \quad \lambda \max_{k=-N/2+1}^{N/2} |m(\omega_k)| \leq K_{\text{RK4}},$$

where $K_{\text{RK4}} = 2\sqrt{2}$ is defined by

$$(89) \quad K_{\text{RK4}} = \max\{b, \text{ where } a + ib \in \mathcal{D}_{\text{RK4}}\} = 2\sqrt{2}.$$

where \mathcal{D}_{RK4} is the domain of stability of the RK4 scheme, [17, Chap. IV.2, p. 18]. The condition (88) is rewritten as

$$(90) \quad \lambda \max_{k=-N/2+1}^{N/2} \left(\frac{\sin\left(\frac{2k\pi}{N}\right)}{\frac{2}{3} + \frac{1}{3} \cos\left(\frac{2k\pi}{N}\right)} \right) \leq K_{\text{RK4}},$$

or equivalently

$$(91) \quad \lambda \leq 2\sqrt{2/3}.$$

We have proved the matrix stability analysis result:

Proposition 4.3. The sequence $(V^n)_{n \geq 0}$ is uniformly bounded under the necessary and sufficient condition

$$(92) \quad \lambda \leq \lambda_\infty, \text{ where } \lambda_\infty = 2\sqrt{2/3}.$$

4.3. Filtered time-scheme. The preceding stability condition is an indication for a bound of the CFL. However it is only valid for the linear equation (66). In the case of a non constant velocity model, the stability must be reinforced. This is of course not surprising, since the basic scheme is centered. A common treatment consists in adding at each time step a so-called high-frequency filter. Refer to [1, 37, 33, 6] and references therein. This filtering step takes the form (see the last line in Algorithm 2 in Section 2.5.

$$(93) \quad V^{n+1} = \mathcal{F} \left(V^n + \frac{\Delta t}{6} \left(K^{(0)} + 2K^{(1)} + 2K^{(2)} + K^{(3)} \right) \right),$$

or equivalently

$$(94) \quad V^{n+1} = \mathcal{F} (r(-\lambda\mathbf{J}) V^n).$$

The so-called filter function \mathcal{F} is the linear operator acting on periodic sequences defined by

$$(95) \quad \mathcal{F}(u_i)_i = \sum_{j=0}^J \frac{a_j}{2} (u_{i+j} + u_{i-j}), \quad 0 \leq j \leq N-1.$$

The width of the stencil is the odd integer $2J + 1$. The first $J + 1$ coefficients a_0, a_1, \dots, a_J must satisfy the $J + 1$ equations

$$(96) \quad \begin{cases} \sum_{j=0}^J a_j = 1, & (a)_0 \\ \sum_{j=0}^J a_j j^{2k} = 0, & k = 1 \dots J - 1, \quad (a)_k \\ \sum_{j=0}^J a_j (-1)^j = 0, & (b) \end{cases}$$

The $J + 1$ equations $(a)_k$, with $k = 0, 1, \dots, J - 1$ translate the consistency with the identity of the filter

Order of accuracy	a_0	a_1	a_2	a_3	a_4	a_5
2	1/2	1/2				
4	10/16	8/16	-2/16			
6	44/64	30/64	-12/64	2/64		
8	186/256	112/256	-56/256	16/256	-2/256	
10	772/1024	420/1024	-240/1024	90/1024	-20/1024	2/1024

TABLE 2. Examples of filters in the form (95) and their orders of accuracy.

function with accuracy $2J$. These relations are obtained by Taylor expansions near x_i . The additional relation 96)b translates that the oscillating mode $\mathbf{v}_j = (-1)^j$ is cancelled out by the operator \mathcal{F} . The linear system (96) is (we drop the dependence in J for simplicity)

$$(97) \quad \mathbf{A}\mathbf{a} = \mathbf{b},$$

where the $\mathbf{a} = [a_0, a_1, \dots, a_J]^T$ is the vector of coefficients in (95), $\mathbf{b} = [1, 0, \dots, 0]^T \in \mathbb{R}^{J+1}$ and \mathbf{A} is the $(J + 1) \times (J + 1)$ matrix

$$(98) \quad \mathbf{A} = \begin{pmatrix} 1 & 1 & 1 & 1 & 1 & 1 & \dots \\ 0 & 2 & 0 & 2 & 0 & 2 & \dots \\ 0 & 1 & 2^2 & 3^2 & 4^2 & 5^2 & \dots \\ 0 & 1 & 2^4 & 3^4 & 4^4 & 5^4 & \dots \\ 0 & 1 & 2^6 & 3^6 & 4^6 & 5^6 & \dots \\ & & & \vdots & \vdots & & \end{pmatrix}.$$

In the following proposition, existence and uniqueness of the coefficients \mathbf{a} is proved.

Proposition 4.4. There exists a unique set $[a_0, a_1, \dots, a_J]$ satisfying the relations (96). The filter function \mathcal{F} in (95) operates on each periodic gridfunction R^k by

$$(99) \quad \mathcal{F}(R^k)_j = P_J(\cos(\theta))R_j^k,$$

where P_J is the polynomial

$$(100) \quad P_J(X) = 1 - \frac{1}{2^J}(1 - X)^J.$$

Moreover, for all periodic gridfunction $(\mathbf{w}_j)_{0 \leq j \leq N-1}$

$$(101) \quad \max_{0 \leq j \leq N-1} |\mathcal{F}(\mathbf{w})_j| \leq \max_{0 \leq j \leq N-1} |w_j|,$$

and the stability condition of the iteration (93) is $\lambda \leq \lambda_J$ where $\lambda_J \geq \lambda_\infty$.

Proof. Existence and uniqueness of a solution of (97) is equivalent to $\det(\mathbf{A}) \neq 0$, Expanding $\det(\mathbf{A})$ along the first column leads to

$$(102) \quad \det(\mathbf{A}) = 2 \sum_{l=1}^{\lfloor \frac{J-1}{2} \rfloor} \Delta_{2l+1},$$

where Δ_l is

$$\Delta_l = \begin{vmatrix} 1 & 2^2 & \dots & (l-1)^2 & (l+1)^2 & \dots \\ 1 & 2^4 & \dots & (l-1)^4 & (l+1)^4 & \dots \\ 1 & 2^6 & \dots & (l-1)^6 & (l+1)^6 & \dots \\ & & & \vdots & \vdots & \\ & & & & & \end{vmatrix} = \frac{((J-1)!)^2}{l^2} \begin{vmatrix} 1 & 1 & \dots & 1 & 1 & \dots \\ 1 & (2^2)^1 & \dots & ((l-1)^2)^1 & ((l+1)^2)^1 & \dots \\ 1 & (2^2)^2 & \dots & ((l-1)^2)^2 & ((l+1)^2)^2 & \dots \\ & & & \vdots & \vdots & \end{vmatrix}.$$

This is equivalent to

$$(103) \quad \Delta_l = \frac{((J-1)!)^2}{l^2} \text{VDM}_{J-1}(1, 2^2, 3^2, \dots, (l-1)^2, (l+1)^2, \dots, J^2).$$

where $\text{VDM}_p(x_1, x_2, \dots, x_p)$ denotes the Vandermonde determinant

$$(104) \quad \text{VDM}_p(x_1, x_2, \dots, x_p) = \prod_{1 \leq l_1 < l_2 \leq p} (x_{l_2} - x_{l_1})$$

Each Vandermonde determinant is positive and therefore in (20), $\det(\mathbf{A}) > 0$, whence the uniqueness of \mathbf{a} , solution of (97).

Consider now the function $z \in \mathbb{C} \mapsto \beta_J(z)$ defined by

$$(105) \quad \beta(z) = \sum_{l=0}^J \frac{a_l}{2} (z^l + z^{-l}),$$

where $\mathbf{a} = [a_0, \dots, a_J]^T$ is the solution of (97). Denoting T_l the l -th Tchebycheff polynomial, it turns out that

$$(106) \quad \beta(e^{i\theta}) = \sum_{l=0}^J a_l \cos(j\theta) = \sum_{l=0}^J a_l T_l(\cos \theta) = P_J(\cos \theta),$$

with

$$(107) \quad P_J(X) = 1 - \frac{1}{2^J} (1 - X)^J.$$

Clearly we have

$$(108) \quad 0 \leq P_J(\cos \theta) \leq 1, \quad 0 \leq \theta < \pi,$$

so that

$$(109) \quad |\beta(e^{i\theta})| \leq 1, \quad 0 \leq \theta < \pi.$$

The stability condition is obtained by substituting in (87) the term $P_J(\cos \theta)r(-\lambda m(e^{i\theta}))$ to the term $r(-\lambda m(e^{i\theta}))$. This gives

$$(110) \quad \lambda \leq \lambda_J,$$

where

$$(111) \quad \lambda_J = \max \left\{ \lambda \in \mathbb{R}^+ \text{ s.t. } \max_{\theta \in [0, \pi)} (|\beta(e^{i\theta})| |r(-\lambda m(e^{i\theta}))|) \leq 1 \right\}.$$

The relation (111) clearly implies $\lambda_\infty \leq \lambda_J$. □

Table 2 reports the values of a series of filter coefficients \mathbf{a}_J [37]. In addition, a set of approximate values of λ_J is reported in Table 3. As expected, the lower J , the higher the maximal CFL number λ_J .

Accuracy of \mathcal{F} , $2J$	λ_J
∞ (no filter)	1.6329
10	1.6883
8	1.7114
6	1.7485
4	1.8156
2	1.9749

TABLE 3. Maximum CFL number λ_J for the vector iteration (94) in term of J , the width of the stencil of the filter function \mathcal{F} . The function $J \mapsto \lambda_J$ is decreasing. The limit value is $\lambda_\infty = 2\sqrt{2/3} \simeq 1.6239$. This limit value corresponds to $J = +\infty$, i.e. the absence of filtering.

5. CONCLUSION

In this paper, we have considered the centered scheme introduced in [10, 11] to approximate convective problems of interest in climatology. The scheme is strongly related to numerical procedure in Computational Aeroacoustics by compact schemes. On the one hand the scheme is centered and a linear filtering is added at each time step, thus making the numerical diffusion minimal. On the other hand, the evaluation of integral quantities to be preserved did not reveal any particular misbehaviour regarding conservation. Overall the numerical results for all the cases tested revealed a sharp fourth order accuracy and very good stability properties. This raises the question to know for which nonlinear flow regime in climatology more advanced filtering such as the ones considered in [9, 39] is mandatory. This important topic is deferred to future work. In gas dynamics simulations, this topics also arises, when considering low Mach number flows. Extension to the ideas presented here to three-dimensional atmospheric flows is a natural perspective.

REFERENCES

- [1] P. Alpert. Implicit filtering in conjunction with explicit filtering. *J. Comput. Phys.*, 44:212–219, 1981.
- [2] A. Arakawa. Computational design for long-term numerical integration of the equations of fluid motion: Two-dimensional incompressible flow. part i. *J. Comput. Phys.*, 1:119–143, 1966.
- [3] L. Bao, R. D. Nair, and H. M. Tufo. A mass and momentum flux-form high-order discontinuous Galerkin shallow water model on the Cubed-Sphere. *J. Comput. Phys.*, 271:224–243, 2014.
- [4] M. Ben-Artzi, J-P. Croisille, and D. Fishelov. Convergence of a compact scheme for the pure streamfunction formulation of the unsteady Navier–Stokes system. *SIAM J. Numer. Anal.*, 44:1997–2024, 2006.
- [5] M. Ben-Artzi, J. Falcovitz, and P.G. LeFloch. Hyperbolic conservation laws on the sphere. A geometry compatible finite volume scheme. *J. Comput. Phys.*, 228:5650–5668, 2009.
- [6] C. Bogey and C. Bailly. A family of low dispersive and low dissipative explicit schemes for flow noise and noise computations. *J. Comput. Phys.*, 194:194–214, 2003.
- [7] C. Chen and F. Xiao. Shallow water model on cubed-sphere by multi-moment finite volume method. *J. Comput. Phys.*, 227:5019–5044, 2008.
- [8] L. Collatz. *The Numerical Treatment of Differential Equations*. Springer-Verlag, 3-rd edition, 1960.
- [9] A.W. Cook and W.H. Cabot. A high-wavenumber viscosity for high-resolution numerical methods. *J. Comput. Phys.*, 195:594–601, 2004.
- [10] J.-P. Croisille. Hermitian compact interpolation on the Cubed-Sphere grid. *Jour. Sci. Comp.*, 57,1:193–212, 2013.
- [11] J.-P. Croisille. Hermitian approximation of the spherical divergence on the Cubed-Sphere. *Jour. Comp. App. Math.*, 280:188–201, 2015.
- [12] P.C. Fragile, C.C. Lindner, P. Anninos, and J.D. Salmonson. Application of the cubed-sphere grid to tilted black-hole accretion disks. *Astrophysical Journal*, 691:482, 2009.
- [13] J. Galewsky, R.K. Scott, and L.M. Polvani. An initial-value problem for testing numerical models of the global shallow water equations. *Tellus*, 56:429–440, 2004.
- [14] S. Ghader and J. Nordström. High-order compact finite difference schemes for the vorticity-divergence representation of the spherical shallow water equations. *Int. J. Numer. Meth. Fluids*, 78:709–738, 2015.
- [15] M. Ghil and S. Childress. *Topics in Geophysical Fluid Dynamics: Atmospheric dynamics, Dynamo theory and Climate Dynamics*. Springer, 1987.
- [16] B. Gustafsson. *High Order Difference Methods for Time Dependent PDE*. Springer-Verlag, 2008.
- [17] E. Hairer and G. Wanner. *Solving Differential equations vol. II*. Springer Series in Comp. Mathematics. Springer-Verlag, 1991.

- [18] G. Hämmerlin and K-H. Hoffmann. *Numerical Mathematics*. Springer-Verlag, 1991.
- [19] B.A. Jones, G.H. Born, and G. Beylkin. Comparisons of the cubed-sphere gravity model with the spherical harmonics. *Journal of guidance, control, and dynamics*, 33:415, sqq, 2010.
- [20] K. K. Katta, R.D. Nair, and V. Kumar. High-order finite-volume transport on the cubed sphere: Comparison between 1d and 2d reconstruction schemes. *Mon. Wea. Rev.*, 143:2937–2954, 2015.
- [21] J. Kim and P. Moin. Application of a fractional-step method to incompressible Navier–Stokes equations. *J. Comput. Phys.*, 59:308–323, 1985.
- [22] S. K. Lele. Compact finite-difference schemes with spectral-like resolution. *J. Comput. Phys.*, 103:16–42, 1992.
- [23] R. D. Nair, H.-W. Choi, and H. M. Tufo. Computational aspects of a scalable high-order discontinuous Galerkin atmospheric dynamical core. *Comput. Fluids*, 38:309–319, 2009.
- [24] R.D. Nair and B. Machenhauer. The mass-conservative cell-integrated semi-lagrangian advection scheme on the sphere. *Mon. Wea. Rev.*, 130:649–667, 2002.
- [25] N. Paldor. *Shallow Water Waves on the Rotating Earth*. Springer Brief in Earth System Sciences. Springer-Verlag, 2015.
- [26] J. Pedlosky. *Geophysical Fluid Dynamics*. Springer, 2nd edition, 1987.
- [27] B. Portelenelle and J.-P. Croisille. An efficient quadrature rule on the cubed sphere. *J. Comp. App. Math*, 328:59–74, 2018.
- [28] C. Jablonowski R. D. Nair. Moving vortices on the sphere: a test-case for horizontal advection problems. *Mon. Wea. Rev.*, 136:689–711, 2008.
- [29] C. Ronchi, R. Iacono, and P. S. Paolucci. The Cubed Sphere: A new method for the solution of partial differential equations in spherical geometry. *J. Comput. Phys.*, 124:93–114, 1996.
- [30] R. Sadourny. Conservative finite-difference approximations of the primitive equations on quasi-uniform spherical grids. *Mon. Wea. Rev.*, 100:136–144, 1972.
- [31] J. G. Simmonds. *A Brief on Tensor Analysis*. Undergraduate Texts in Math. Springer, 2nd edition, 1994.
- [32] A. St-Cyr, C. Jablonowski, J.M. Dennis, H.M. Tufo, and S.J. Thomas. A comparison of two shallow-water models with nonconforming adaptive grids. *Month. Weath. Rev.*, 136:1898–1922, 2008.
- [33] C. K. W. Tam and J. C. Webb. Dispersion-relation-preserving finite difference schemes for computational acoustics. *J. Comput. Phys.*, 107:262–281, 1993.
- [34] J. Thuburn and Y. Li. Numerical simulation of rossby-haurwitz waves. *Tellus*, 52A:181–189, 2000.
- [35] P. A. Ullrich, C. Jablonowski, and B. van Leer. High order finite-volume methods for the shallow-water equations on the sphere. *J. Comput. Phys.*, 229:6104–6134, 2010.
- [36] P.A. Ullrich. *Atmospheric Modeling with High-Order finite volume methods*. PhD thesis, The Univ. of Michigan, 2011.
- [37] M. R. Visbal and D. V. Gaitonde. On the use of higher order finite difference schemes on curvilinear and deforming meshes. *J. Comput. Phys.*, 181:155–185, 2002.
- [38] D.L. Williamson, J.B. Drake, J.J. Hack, R. Jakob, and P. N. Swarztrauber. A standard test set for numerical approximations to the shallow water equations in spherical geometry. *J. Comput. Phys.*, 102:211–224, 1992.
- [39] H.C. Yee and B. Sjögren. Designing adaptive low-dissipative high-order schemes for long-time integrations. volume 66 of *Turbulent Flow Computation, Fluid Mechanics and its Applications*. Kluwer Acad. Pub., 2004.

†UNIVERSITÉ DE LORRAINE, DÉPARTEMENT DE MATHÉMATIQUES, F-57045 METZ, FRANCE, ‡C.N.R.S., INSTITUT ELIE CARTAN DE LORRAINE, UMR 7502, F-57045 METZ, FRANCE
E-mail address: matthieu.brachet@univ-lorraine.fr, jean-pierre.croisille@univ-lorraine.fr